Geothermics 103 (2022) 102431

Contents lists available at ScienceDirect

Geothermics

journal homepage: www.elsevier.com/locate/geothermics

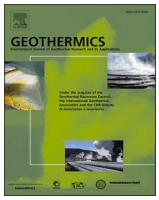

Regional thermal anomalies derived from magnetic spectral analysis and 3D gravity inversion: Implications for potential geothermal sites in Tanzania

Makoye Mabula Didas [a,f,g,*], Egidio Armadillo [b], Gylfi Páll Hersir [c], William Cumming [d], Daniele Rizzello [e]

[a] Tanzania Geothermal Development Company Ltd (TGDC), P. O. Box: 14801, Ursino House No. 25, Dar es Salaam, Tanzania
[b] Applied Geophysics Laboratory, University of Genoa, Italy
[c] gylfi.pall@outlook.com, Iceland
[d] Cumming Geoscience, Santa Rosa, CA, USA
[e] Tellus S.A.S., Italy
[f] Faculty of Earth Sciences, University of Iceland, Sturlugata 7, Reykjavík 101, Iceland
[g] GRÓ-GTP, Urðarhvarfi 8 (B), Kópavogi 203, Iceland

ARTICLE INFO

Keywords:
East African rift system
Aeromagnetic data
Gravity data
Centroid method
Curie point depth
Moho depth
Heat flow

ABSTRACT

Tanzania is one of the several countries intersected by the East African Rift System (EARS) endowed by a geothermal potential that has been explored only to a limited extent. Here we present the first heat flux map over the region based on the Curie point depth (CPD) estimation from aeromagnetic data. We have estimated the base of magnetic sources as a proxy for the CPD from the radially average power spectra of the total magnetic field using the centroid and the de-fractal methods. Our results show that the CPDs range ca. 11 to 43 km and are comparable to, but more detailed than global CPD estimates. The heat flow has then been computed assuming a constant thermal conductivity. In order to evaluate the results against crustal thickness, we have inverted the gravimetric regional field data constrained by the existing Moho depth from seismic receiver functions. Our analysis has revealed high heat flow values (over 100 mW/m^2) along the EARS and at the Proterozoic collision boundaries that have been reactivated by the EARS. In general, the high heat flow anomalies coincide with known surface geothermal manifestations and shallow Moho depth in the range ca. 30 to 35 km. A high heat flow anomaly is also found in the central part of the Tanzanian craton, likely related to the mantle plume imaged by seismic tomography. The most interesting areas for geothermal exploration in Tanzania, according to our results, are the EARS triple junction in the Rungwe volcanic province, the north Tanzania divergent zone and the areas of the Proterozoic collision boundaries reactivated by the EARS.

1. Introduction

Understanding the thermal structure of the Earth's crust is essential in geothermal exploration and development. Although the *in-situ* crustal thermal gradient can be measured directly by drilling deep boreholes (Nyblade et al., 1990; Nyblade and Pollack et al., 1993; Nyblade, 1997), estimation of the thermal gradient and heat flow at a regional scale using direct methods alone suffers from many drawbacks such as high cost, non-uniform distribution, limited investigation depth and disturbed temperatures due to shallow groundwater circulation. One of the most commonly used indirect method to characterize regional heat flow is based on estimation of the depth to the base of the magnetic sources (DBMS) from spectral analysis of the total magnetic intensity anomalies. In many cases, DBMS can be used as a proxy for the Curie point depth (CPD) in the Earth's crust. The CPD is the depth at which magnetic minerals, principally magnetite, in the Earth's crust lose their magnetic properties when temperature increases above their Curie temperature of about 580°C (Hunt et al., 1995). Once the CPD has been estimated over an area, it can be used to map the geothermal gradient and the heat flux, assuming mean values for the thermal conductivity.

Aside from uncertainty in the computation of DBMS from magnetic spectra, significant sources of uncertainty in the estimation of

* Corresponding author at: Tanzania Geothermal Development Company Ltd (TGDC), P. O. Box: 14801, Ursino House No. 25, Dar es Salaam, Tanzania.
E-mail address: geodidas@ymail.com (M.M. Didas).

https://doi.org/10.1016/j.geothermics.2022.102431
Received 16 August 2021; Received in revised form 14 April 2022; Accepted 21 April 2022
Available online 4 May 2022

temperature gradient in this study include the assumption that the DBMS is controlled only by temperature (at the CPD) and the assumption that heat transfer from CPD to the surface is only by 1D conduction. In addition to temperature, the DBMS can be controlled by lateral variations in lithology with differing magnetic properties (Bansal et al., 2011; Ross et al., 2006). The assumption of 1D conduction may not be valid where the lithosphere thins in rift zones, likely causing significant 2D, 3D or transient conductive and/or convective heat transfer, for example in geothermal reservoirs. Therefore, it is important to interpret the DBMS/CPD and geothermal gradient estimates in the context of alternative constraints provided by the tectonic setting, hydrologic regime, temperature measurements from deep boreholes, crustal

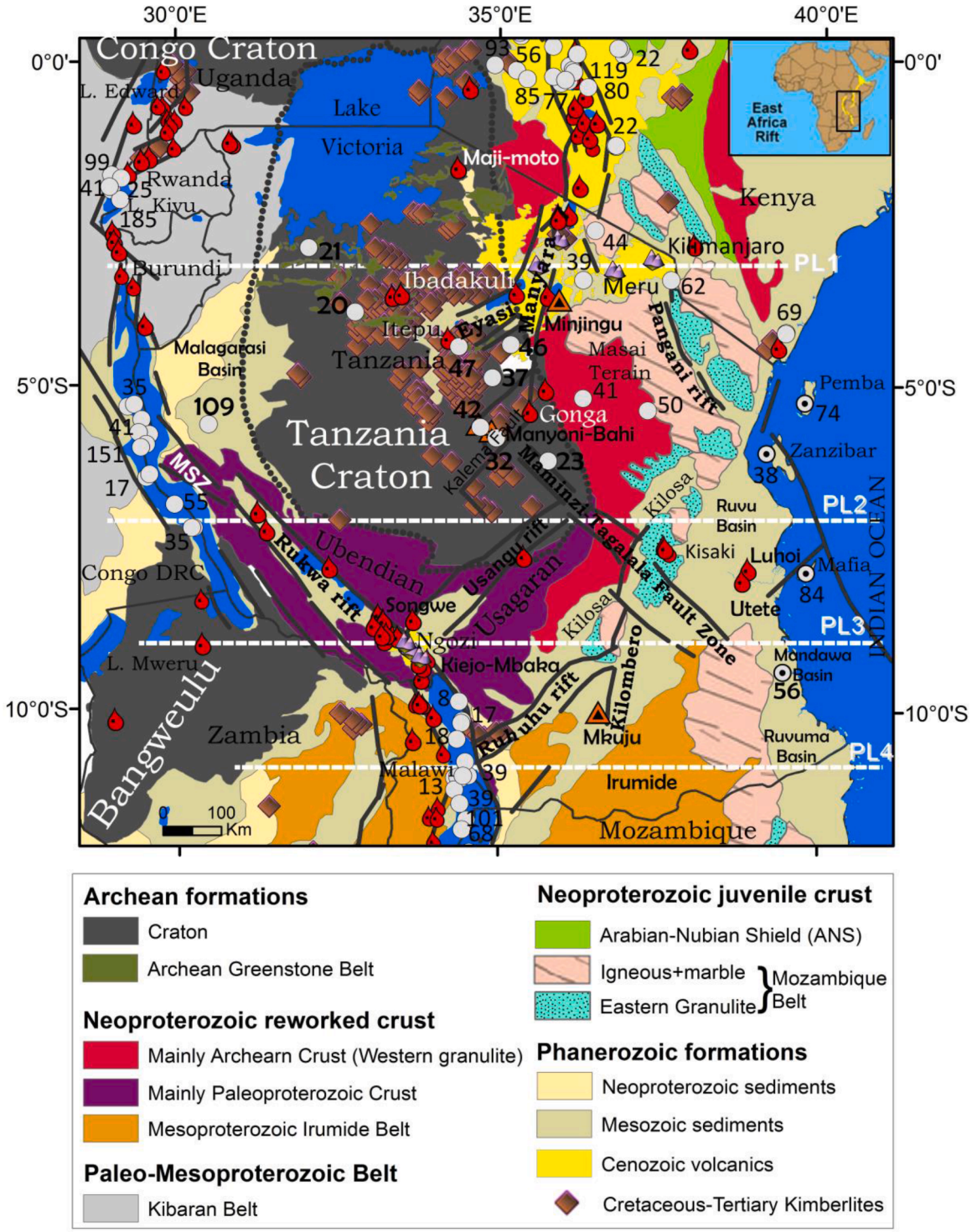

Fig. 1. Geological map of Tanzania and neighbouring countries showing the main geological domains with the EARS margins shown as thick black segment lines. The white numbered circles are boreholes and the numbers displayed are the heat flux in mW/m^2. The red drops are hot springs. The brown diamonds are the Cretaceous-Tertiary Kimberlite pipes. Map modified from Fritz et al. (2013). The continuous thin black lines define the political boundaries. The white dotted lines are selected profiles for the integrated interpretation of the results shown in Fig. 9.

boundaries derived from seismic and gravity measurements, and the properties of geologic formations, including their magmatic age, radiogenic heating, thermal conductivity and magnetic parameters. In spite of such complications, similar CPD and thermal gradient estimates have been used to complement borehole thermal data worldwide where deep boreholes are unavailable or leave very wide gaps, for example in: northeast Japan (Okubo and Matsunaga, 1994); Yellowstone National Park, U.S.A. (Bhattacharya and Leu, 1975); Kyushu Island, Japan (Okubo et al., 1985); east and southeast Asia (Tanaka et al., 1999); the African-Eurasian convergence zone in southwest Turkey (Dolmaz et al., 2005); south-central Europe (Chiozzi et al., 2005); California, U.S.A. (Ross et al., 2006). More recent examples include Australia (Kumar et al., 2021); East Africa beneath the Malawi rift zone (Njinju et al., 2019); Western U.S.A. (Bouligand et al., 2009); Greenland (Martos et al., 2018); Yukon, Canada (Witter et al., 2018); Antarctica (Martos et al., 2017, 2019; Dziadek et al., 2021); in the Adriatic Sea, Eastern Italy (Kelemework et al., 2021); Colombian Caribbean (Quintero et al., 2019) and Mexico (Carrillo-de la Cruz et al., 2020a, 2021).

Tanzania is one of the several countries intersected by the East African Rift System (EARS) with geothermal potential that has been explored only to a limited extent (Hochstein et al., 2000; Mnjokava et al., 2015). A first attempt to study the regional heat flow in Tanzania was made on the basis of several shallow boreholes (70–300 m deep), sparsely scattered in the craton and the surrounding Proterozoic orogenic belts (Nyblade and Pollack, 1993; Nyblade, 1997). The results indicate heat flow ranges of 60-74, 39–62 and 20–47 mW/m^2 in the Mesoproterozoic Kibaran belt, Neoproterozoic Mozambique belt and in Archean Tanzanian craton, respectively. Heat flow of 56 mW/m^2 was obtained from an onshore deep hydrocarbon exploration well and 51-87 mW/m^2 further east offshore (Nyblade, 1997). An inferred average, maximum and minimum surface heat flow value of 106 ± 51, 68 ± 47, and 53 ± 19 mW/m^2 in the eastern rift (largely in the Kenyan rift), western rift and the surrounding shield, respectively, was estimated from shallow boreholes (Fadaie and Ranalli, 1990). Location and values of the direct available measurements are shown in Fig. 1. Note that the locations are very scattered and focused on known anomalous areas. Therefore, these measurements cannot be used to obtain a representative regional heat flux map. Also, these data may be strongly biased by shallow water circulation (Nyblade et al., 1990; Nyblade and Pollack, 1993). In recent years, the geothermal potential of Tanzania has been investigated through several internationally funded projects focusing on a few promising prospect areas (Hersir et al., 2015; Kabaka et al., 2016): the Songwe, Kiejo-Mbaka and Luhoi low-medium temperature geothermal systems (Hinz et al., 2018; Armadillo et al., 2020; Rizzello et al., 2018) and the high-temperature Ngozi prospect (Kalberkamp et al., 2010; Alexander et al., 2016; Didas and Hersir, 2021). However, a regional heat flux map covering the whole of Tanzania and the associated detailed tectono-thermal interpretations are still lacking.

The goal of this study is to produce a heat flux map of Tanzania by integrating the existing direct measurements with CPD estimations from the DBMS to assess geothermal development potential in the context of the geology of the region. The geology of Tanzania is dominated by the Tanzania Archean Craton which is bordered by Proterozoic orogenic belts associated with Gondwana amalgamation and is crosscut by the Cenozoic EARS (Fig. 1). Mesozoic sediments cover the Neoproterozoic belt to the east. To support a new DBMS computation, we have merged two magnetic data sets, the total intensity aeromagnetic data acquired in Tanzania from 1977 to 1980 (Stendal et al., 2004) and magnetic data from the 2 arc-minute Earth Magnetic Anomaly Grid (EMAG2) described by Meyer et al. (2017). Using the centroid method of Okubo et al. (1985) and Tanaka et al. (1999) and the de-fractal method (Salem et al., 2014), we have computed the DBMS from spectral analyses of magnetic anomalies. Heat flow is then estimated by assuming conduction from the CPD to the surface, assuming a reasonably close match of the DBMS to the CPD. To further constrain the potential for new geothermal prospects, we have integrated existing crustal thickness estimations from passive seismic data with 3D gravity inversion to obtain the Moho interface and better constrain how the CPD, heat flow and known geothermal sites are correlated with seismic and tectonic information. To provide a validation benchmark, we have compared the heat flow estimates from CPD to the geothermal gradient found in deep hydrocarbon exploration wells and analysed the relationship between the heat flow anomalies and the location of uranium deposits.

2. Geological and tectonic setting

The geology of Tanzania consists of Archean cratonic nuclei also known as the Tanzanian craton (Borg and Krogh, 1999; Manya and Maboko, 2003) which is surrounded by the Proterozoic orogenic belts formed as a result of widespread continental collisions during Gondwana amalgamation (Boniface et al., 2012; Thomas et al., 2016). The last collision is marked by the north-south trending Neoproterozoic Pan African orogenic belt (Mozambique belt) that forms the East African orogen (Fig. 1, Meert and Lieberman, 2008; Boniface, 2019). In Permo-Triassic time, the East African orogen was overprinted by phases of post-orogenic extension which resulted in the formation of deep intracratonic NE-SW trending Karoo basins (Fig. 1) and initiation of coastal basins (Nicholas et al., 2007). In the Jurassic-Cretaceous some of the Karoo rifts were reactivated leading to the successful rifting that separated Madagascar from East Africa and to the development of the continental passive margin along the western coast of the Indian Ocean (Reeves and De Wit, 2000; Bumby and Guiraud, 2005). From Neogene to the present, the craton and the Proterozoic orogenic belts are overprinted by the EARS (Saria et al., 2014; Asefa and Ayele, 2020).

2.1. The Archean Tanzanian craton

The Tanzanian craton extends from central Tanzania to south Uganda and Kenya and adjoins the Congo craton to its north (Fig. 1). It is composed of orthogneiss basement dated >3600 Ma intruded by large granitoid plutons dated between 2610 and 2815 Ma (Kabete et al., 2012b; Thomas et al., 2016). The emplacement of granitic bodies was coeval with the basaltic volcanic rocks erupted in an intra-oceanic setting (Manya, 2001; Manya and Maboko, 2003), metamorphosed to greenschist facies (Tanzania greenstone belts) that hosts world-class gold deposits (Kabete et al., 2012a). During the Cretaceous and Tertiary, over 360 Kimberlite pipes intruded the Tanzanian craton (Stiefenhofer and Farrow, 2004), including the youngest known Kimberlite (>30 Ma) located in the western side of the craton (Fig. 1, Brown et al., 2012). The craton margins are tectonically sutured to adjacent formations by Proterozoic orogenic belts. The NW-SE trending Paleoproterozoic Ubendian belt limits the craton to the southwest (Manya, 2011; Boniface and Appel, 2017). The NE-SW trending Paleoproterozoic Usagaran belt borders it to the south (Thomas et al., 2016), the Mesoproterozoic Kibaran belt limits it to the west and the N-S trending Neoproterozoic Mozambique belt borders it to the east (Fritz et al., 2013; Thomas et al., 2016; Boniface, 2019). The Ubendian belt lies along a successful branch of a Mesoproterozoic rift that opened to form ocean basins between the Tanzanian craton and Bangweulu block (Boniface, 2019). From Neogene onwards, the eastern branch of the EARS has impinged across the eastern and southern margins of the Tanzanian craton (Ebinger et al., 1997; Saria et al., 2014; Ebinger et al., 2017).

2.2. Proterozoic orogenic belts

The Paleoproterozoic Ubendian-Usagaran orogenic belts are comprised of medium to high-grade metamorphic rocks, granitic and gabbroic intrusions, and volcanic rocks (Lenoir et al., 1994; Mruma, 1995) formed as a result of subduction and tectonic collision events caused by Gondwana amalgamation in Tanzania (Boniface, 2019). The Neoproterozoic Mozambique belt comprises juvenile rocks including the nappes of anorthosite-gabbro suites with emplacement ages between

700 and 900 Ma. They had subsequently been metamorphosed to amphibolite to granulite facies between 620 and 550 Ma (Möller et al., 2000; Kröner et al., 2003; Thomas et al., 2014), corresponding to the tectono-thermal events of the East African Orogen (Sommer and Kröner, 2013) resulting from the closure of the Mozambique Ocean between 850 and 620 Ma (Fritz et al., 2013; Mole et al., 2018). The East African Orogen extends from southern Israel, Sinai and Jordan in the north to Mozambique and Madagascar in the south (Stern, 1994; Fritz et al., 2013). The late Paleozoic–Mesozoic Karoo sedimentary basins developed in the Paleo-Mesoproterozoic crust (Wopfner, 2002) and the Mozambique belt which is overlaid by the Mesozoic passive-margin coastal sedimentary basins (Fig. 1, Kent et al., 1971). The Paleozoic-Mesozoic sediments have a significant role in the geology of geothermal prospects including a clay cap and/or reservoir in Songwe (Alexander et al., 2016; Hinz et al., 2018), Ngozi (Alexander et al., 2016), Kiejo-Mbaka (Rizzello et al., 2018) and Luhoi (Armadillo et al., 2020) prospects. From Neogene onwards, the EARS has disrupted the Proterozoic orogenic belts.

2.3. Mesozoic rifting

The Mesozoic rift consists of the deep intracratonic NE-SW trending Karoo Basins (e.g., Ruhuhu, Kilombero and Kilosa basins, Fig. 1) and the southeast coastal Basins of Tanzania (Nicholas et al., 2007). They were formed as a result of the breakup of Gondwanaland from Permian to Late-Cretaceous (Bumby and Guiraud, 2005) and the development of the passive continental margin along the western margin of the Indian Ocean (Kent et al., 1971; Bussert et al., 2009). The coastal and offshore sedimentary basins consist of marine and terrestrial sediments over 4000 m thick (Didas, 2016) that host a potential hydrocarbon system (Kagya, 1996), with discoveries of natural gas totaling more than 57 TCF (TPDC, 2021).

2.4. The East Africa rift system (EARS)

The Cenozoic EARS consists of two branches, the western rift with scant magmatic eruption products (Ebinger, 1989) and the eastern branch with much more prolific magmatic eruption activity (Foster et al., 1997; Ebinger et al., 2017). The eastern branch starts at the Afar

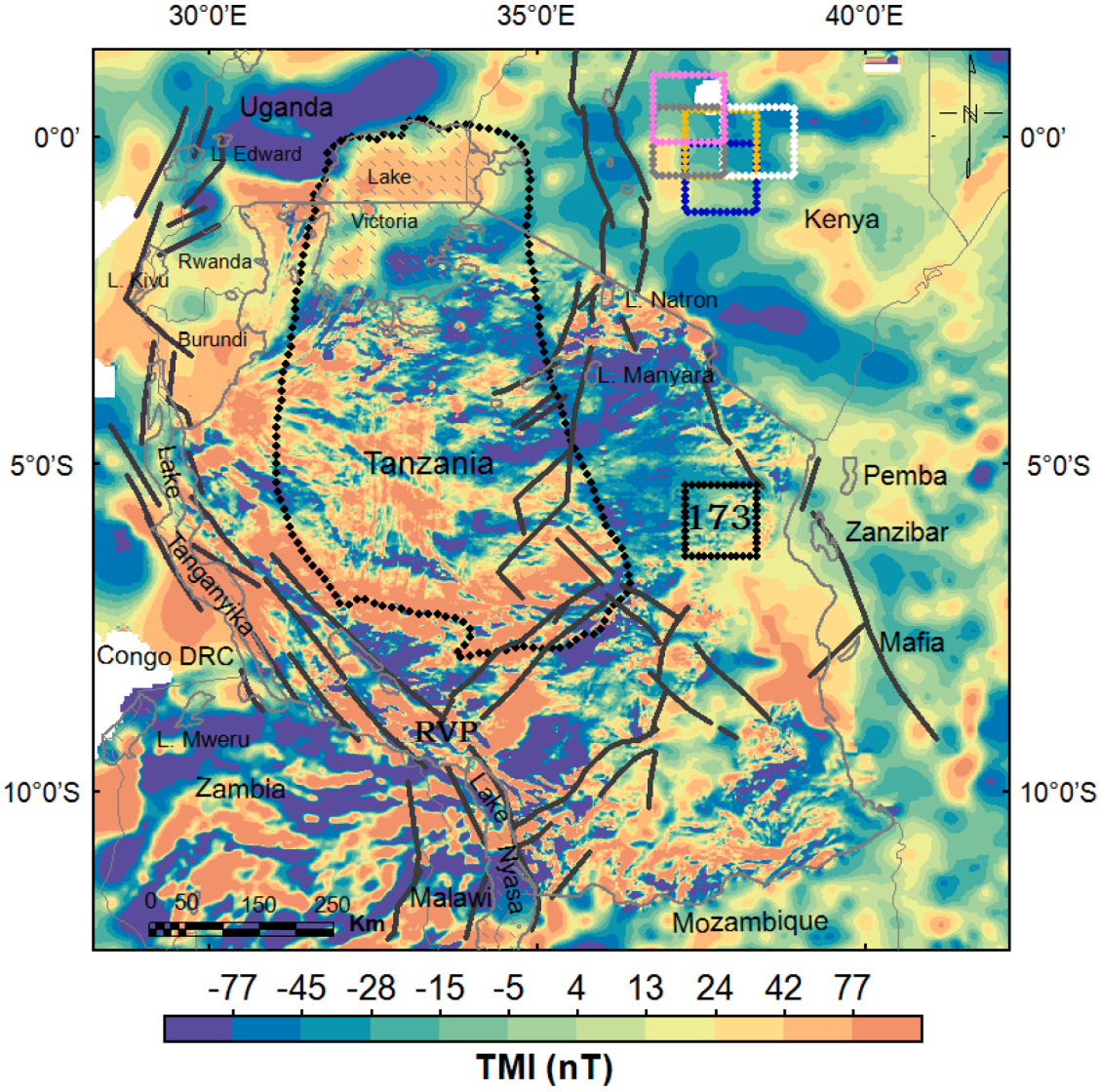

Fig. 2. TMI map of Tanzania and neighbouring countries merged from EMAG2 (Meyer et al., 2017) and 1977-1980 surveys (Stendal et al., 2004). The area was divided into 447 overlapping square windows, each with a dimension of 110 × 110 km^2 (1°x1°) used for the computations of the power spectra. The purple, grey, yellow, blue and white windows in the NE (upper right) corner represent how the windows overlap at 50%. The black square shows the location of window 173 with the computed 1D radially power spectrum shown in Fig. 3. The Tanzanian craton is outlined with a dotted black line. Thick black segment lines indicate the EARS.

triple junction in southeast Eritrea and north Ethiopia and is developed mostly within the Neoproterozoic Mozambique belt (Fig. 1). The rift stretches to the south through Ethiopia, Kenya and north Tanzania where it forms the north Tanzania divergent zone (NTDZ) defined by the Manyara and Eyasi rift zones that extends into the Archean craton (Fig. 1). The western branch stretches from northern Uganda within the Ruwenzori belt and extends south along pre-existing structures in the Mesoproterozoic Kibaran belt and further south along the Ubendian-Craton suture through the Irumide belt in Malawi and central Mozambique (Fig. 1, Ebinger et al., 1989). South of the Tanzanian craton and southwest of the Ubendian belt, the EARS has reactivated Karoo aged faults within the Mesozoic Karoo rifts (Le Gall et al., 2004). In Tanzania, the eastern and western branches of the EARS converge in the Mbeya area forming a triple junction within the Rungwe Volcanic Province (RVP, Fontijn et al., 2012), and then form the N-S trending Malawi rift which extends further south to Malawi and Zambia where it terminates. Recent seismological studies (e.g., O'Donnell et al., 2013; Mulibo and Nyblade, 2016) have proposed inferred extension of the eastern branch through the Neoproterozoic Mozambique belt crossing the Tanzanian coastal basins.

3. Geophysical data and methods

3.1. Aeromagnetic data

We have used the total magnetic intensity (TMI) airborne anomaly data (Fig. 2) collected by Geosurveys in 1977 and 1980 along E-W flight lines spaced 1 km apart, sampled every 50 m and draped at 120 m nominal ground clearance over large parts of Tanzania (Stendal et al., 2004). No data were collected over Lake Victoria and the Kilimanjaro and Uluguru mountains to the north, northeast and east, respectively. Hence, we have used the TMI Earth Magnetic Anomaly Grid 2-arc-minute resolution (EMAG2) dataset as a supplement for the uncovered areas. EMAG2 are open-source global TMI datasets compiled from satellite, ship, and airborne magnetic measurements and merged into a 2-arc-minute grid upward continued at 4 km above the geoid (Meyer et al. (2017). These data were draped to an elevation of 120 m using the ETOPO1 global relief model data with 1-arc-minute resolution (Amante and Eakins, 2009) and merged with the TMI of the 1977–1980 survey (Fig. 2). The two magnetic grids have been merged using the Knit Grids utilities in the Seequent Geosoft Oasis Montaj package. Along the suture line, the mismatch in the grid values is corrected by adjusting the grids on either side of the path, propagating the correction required at each suture point in a circle whose radius is equal to the user-defined correction width. This method provides smooth blending without over-smoothing high-frequency variations which may occur along the suture path. The final grid was sampled at 250 m spacing.

3.2. Curie point depth (CPD) estimation methodologies

The depth to the bottom of the magnetic sources (DBMS) can be used as a proxy for the Curie point depth (CPD), where temperature becomes so high that magnetic minerals in the Earth's crust lose their magnetic properties (Okubo et al., 1985). The most common magnetic mineral in the Earth's crust is magnetite, an oxide of iron but other metals influence the magnetic properties of minerals, including copper, cobalt, manganese, magnesium and nickel, causing the Curie temperature to vary from 440 to 580°C (Hunt et al., 1995). However, because magnetite is the dominant magnetic mineral, its Curie temperature of ~ 580°C is usually assumed to be the reference temperature for the CPD (Hunt et al., 1995; Ross et al., 2006). The assumption of DBMS as a proxy for CPD may be biased for many reasons. For instance, DBMS may be related to a contrast in lithology such as sub-horizontal detachment faults or unconformity or contact between young volcanic rocks overlying weakly magnetic thick sedimentary rocks (Bansal et al., 2011; Ross et al., 2006) or its computation could be distorted by the window size of the data used to compute the power spectrum (Ravat et al., 2007). Therefore, additional independent geothermal, geological and geophysical data are usually needed to verify the correspondence between DBMS and CPD (Okubo et al., 1985).

There are several methods to estimate the DBMS from magnetic anomalies, as described for instance in Carrillo-de la Cruz et al. (2020a) and Kelemework et al. (2021). In this study, we have used the centroid method (Okubo et al., 1985; Tanaka et al., 1999) and evaluated the results against the de-fractal method (Salem et al., 2014). All the methods work in the frequency domain and use the low wavenumbers (long wavelength) part of the spectrum, assuming that they are related to the deep magnetic sources (Spector and Grant, 1970; Bhattacharya and Leu, 1975).

The theoretical 2D spectrum of the total magnetic field for a random and uncorrelated distribution of magnetization (P_t) is presented by Blakely (1995) as a function of magnetization power spectrum (P_m), top depth (Z_t) and bottom depth (Z_b) of the anomalous body.

$$P_t(k_x, k_y, Z_t, Z_b) = 4\pi^2 C_m^2 P_m(k_x, k_y)|\Theta_m|^2|\Theta_f|^2 e^{-2|k|Z_t}\left(1 - e^{-|k|(Z_b - Z_t)}\right)^2 \quad (1)$$

In Eq. (1), C_m is a proportionality constant that depends on the direction of magnetization and geomagnetic field, k_x, k_y are the wavenumbers in 2π radian/km in the x and y directions, respectively. Their Euclidean norm k is expressed as $|\mathbf{k}| = \sqrt{k_x^2 + k_y^2}$, and Z_t and Z_b are the depths to the top and bottom, respectively, of the magnetic source assumed to be a slab. Finally, Θ_m and Θ_f are the directional factors related to the magnetization and geomagnetic field, respectively. When the 1D radially averaged power is computed, the terms Θ_m, Θ_f and $P_m(k_x, k_y)$ become constant. Hence, the power spectrum is expressed as:

$$P(k, Z_t, Z_b) = A_1 e^{-2|k|Z_t}\left(1 - e^{-|k|(Z_b - Z_t)}\right)^2 \quad (2)$$

where, P is the 1D power spectrum and A_1 is a constant.

In terms of centroid depth Z_0, (i.e., the midpoint between the top and bottom of the magnetic source) Eq. (2) can be written as (Okubo et al., 1985; Tanaka et al., 1999):

$$P(k, Z_t, Z_o, Z_b) = A_2 e^{-|k|Z_0}\left(e^{-|k|(Z_t - Z_0)} - e^{-|k|(Z_b - Z_0)}\right) \quad (3)$$

where A_2 is a constant.

For low wavenumbers of the radially averaged amplitude spectra Eq. (3) can be written as (Tanaka et al., 1999):

$$\ln\left(\frac{(P(k))^{\frac{1}{2}}}{k}\right) = A_3 - |k|Z_0 \quad (4)$$

where A_3 is constant. The centroid depth Z_0 can, therefore, be calculated from the slope of the low wavenumber segment of the spectrum.

For the depth to the top of the magnetic source Z_t, which normally is obtained in the medium to high wavenumber range of the spectrum, Eq. (3) can be written as (Spector and Grant, 1970),

$$\ln(P(k))^{\frac{1}{2}} = A_4 - |k|Z_t \quad (5)$$

where, A_4 is a constant.

Then the approach of Okubo et al. (1985) and Tanaka et al. (1999) is used to calculate the DBMS or Z_b.

$$\text{DBMS} = (2Z_o - Z_t) \quad (6)$$

where, Z_o is the centroid depth of the magnetic source and Z_t is the depth of the top.

In the de-fractal method, Salem et al. (2014) assumed that the observed amplitude A_F spectrum may be corrected considering the fractal sources using the relationship:

$$A_R(K_x, K_y) = A_F(K_x, K_y)\ K^{\alpha/2} \quad (7)$$

where K is the norm of the wavenumber and α is the fractal parameter. The method evaluates Z_t, Z_b and α computing the forward modeling and evaluating the match between the modeled and corrected spectrum, albeit with high fractal parameter α values tending to overcorrect the spectrum (Carrillo-de la Cruz et al., 2020b).

In this study, we have estimated CPD using both the centroid method (Okubo et al., 1985; Tanaka et al., 1999) and the de-fractal method (Salem et al., 2014). For the centroid method computations, we have used the frequency domain algorithms available in the MagMap Seequent Geosoft Oasis Montaj package. For the de-fractal method computations, we have used the MAGCPD package (Carrillo-de la Cruz et al., 2020b).

3.3. CPD computations by the centroid method

We have applied the centroid method (Okubo et al., 1985; Tanaka et al., 1999) to square windows of dimension 110 km × 110 km (ca. 1° × 1°) running over the study area with 50% overlap. The CPD estimation has been performed on a total of 447 windows. In the case of windows with resulting DBMS larger than 25 km (8% of the total), we have used larger size windows of dimension 220 km × 220 km (ca. 2° × 2°).

The size of the windows has been chosen on the basis of the following

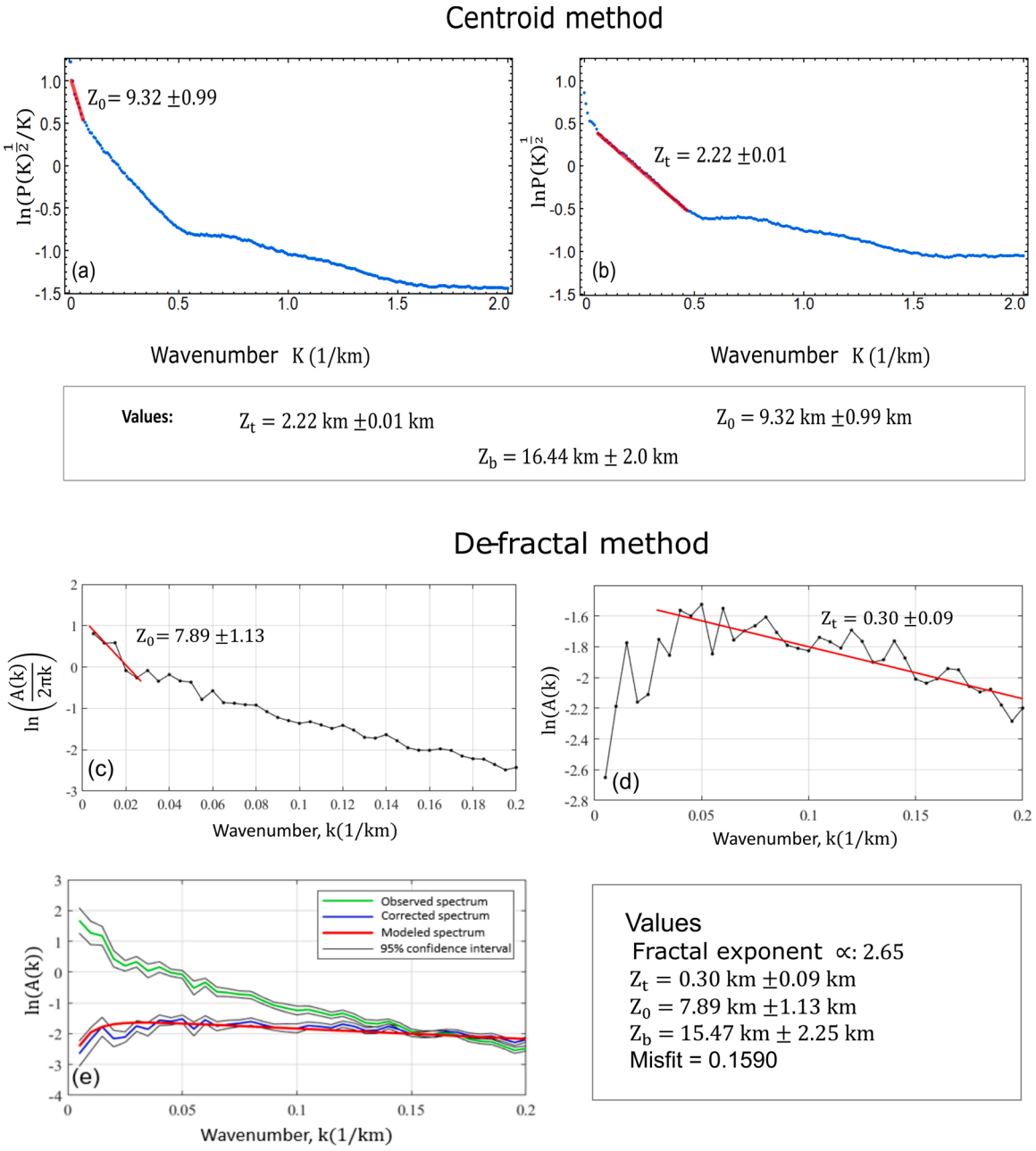

Fig. 3. 1D radially averaged power spectrum and computed parameters for window 173, indicated with black square in Fig. 2. (a) the mean centroid depth (Z_0), (b) mean top depth (Z_t) of the magnetic sources, over the window, respectively, as estimated from the slope of the interpolated red line. Its corresponding CPD (Z_b) is 16.44 ± 2.0 km. Images (c-e) indicate the same parameters in a large window (200 km) centered at the same location as 173 and computed using de-fractal method. The two methods reproduce similar CPD results. For the de-fractal method, the 2.65 fractal parameter produced a good match and minimum misfit between the observed and modeled spectra. The error between the corrected and modeled spectrum is computed as 95% confidence interval represented by the greyish curves in panel 3e.

considerations:

(i) As small as possible window size is essential in order to detect the expected short CPD wavelength variations across the EARS.
(ii) The 110 km window size was used in a similar work by Njinju et al. (2019), who applied the same methodology along the Malawi Rift, just to the south of Tanzania.
(iii) It has been proposed recently by Kelemework et al. (2021) that for the centroid method the window size should be between 3–5 times the average depth of investigation. We, therefore, expect reliable results for CPD depth up to 22 (110/5) to 36.6 (110/3) km, that is up to about 30 km using the 110 km size window, while for the 220 km size window we expect reliable results up to at least CPD of 44 km.

The optimum window size is still a matter of scientific discussion (e.g., Blakely, 1995; Maus et al., 1997; Ravat et al., 2007; Bouligand et al., 2009; Bansal et al., 2011; Li et al., 2013; Abraham et al., 2014; Nwankwo, 2014; Andrés et al., 2018) and is in general unique for each area (Kumar et al., 2020; Ravat et al., 2007). It is small over tectonically active areas with high heat flow and large in stable regions such as the cratonic areas (Ravat et al., 2007; Kelemework et al., 2021). A typical approach is to choose a window large enough to show a clear peak in the very low wavenumber band of the spectrum (e.g. Ravat et al., 2007). We tested different window sizes, such as 500, 400, 300, 250, 220, 110 km. However, the peak was never been clearly detected, possibly because of the presence of a uniformly magnetized layer, a spectral peak represented by a single point, presence of layered sources (Blakely, 1995; Ravat et al., 2007) or the method used to generate the power spectrum (Bansal et al., 2006). The absence of a spectral peak has also been reported by Ravat et al. (2007) and Bouligand et al. (2009) and no peak is visible in the spectra shown in Carrillo-de la Cruz et al. (2020a). Our final choice of a 110 km window is justified because temperature gradients measured in deep petroleum exploration wells are in the range of 22–58 °C/km in different geologic settings of Tanzania (Fig. 6a). Assuming a Curie temperature of 580°C, this range implies a maximum CPD of 26.4 km. Because this value is <30 km our 110 km window size (approximately 4 times the maximum CPD) seems to be suitable.

The selection of the wavenumber bands for the computation of Z_t and Z_0 in each window was based on a physical inspection of the spectra of the respective window (e.g. Bansal et al., 2011). After the reconnaissance of the evident linear features in each plot, a straight line was fitted based on the least-squares method. Therefore, the wavenumber band where the fit is performed varies from plot to plot for each window. Fig. 3a,b show an example of linear fitting for window 173. Considering all the windows, the centroid depths Z_o were estimated from the slope of the spectrum in the wavenumber range 0.0079-0.079 1/km, while the average depths to the top of the magnetic sources Z_t were estimated within the wavenumber range 0.0794-0.5 1/km.

We have also to underline that, in estimating the depths to the top and bottom of the magnetic sources, the centroid method assumes a random and uncorrelated distribution of the magnetic sources (e.g. Spector and Grant, 1970). This hypothesis has been questioned by many authors who have suggested that a fractal/scaling distribution of the magnetic sources would be more realistic (Pilkington and Todoeschuck, 1990, 2004; Maus and Dimri, 1995; Salem et al., 2014). Hence, a scaling exponent has been proposed to be applied to the power spectrum to account for the random magnetization and geological variability (Bansal and Dimri, 1999, 2001, 2005, 2010; Pilkington and Todoeschuck, 1993; Maus and Dimri, 1995; Dimri 2000; Dimri et al., 2003; Bansal et al., 2006). Kelemework et al. (2021) have observed that the centroid method assumption of random and uncorrelated distribution of the sources usually overestimates the CPD. Therefore, the results from this method could be interpreted as a likely deeper limit of the DBMS estimates of the CPD (Fig. 5b). Therefore, the centroid method continues to be used (e.g. Njinju et al., 2019; Dziadek et al., 2021) since it avoids the arbitrary choice of the fractal parameter and is relevant to cases where a deeper range of the CPD is of interest, for example, in areas of cratonic crust like much of Tanzania.

3.4. CPD computations by the de-fractal method

In order to overcome the simplifying assumption of random and uncorrelated magnetic sources, we have applied the de-fractal method (Salem et al., 2014; Carrillo-de la Cruz et al., 2020a) to square windows of 300 and 200 km size covering the study area with 50% overlap. The size of the windows in this approach is larger than in the previous one, because according for instance to Kelemework et al. (2021), it must be larger than minimum 5 times the expected CPD. Since the use of 300 and 200 km windows gave very similar results, we consider here the results obtained with the use of the 200 km size window, giving the higher lateral resolution (Fig. 5a).

The fractal exponent of the de-fractal method allows the user to take into account different magnetization distributions linked to different geological conditions (e.g., Bouligand et al., 2009; Carrillo-de la Cruz et al., 2021). On the other hand, the major drawback with this approach is that the choice of the fractal parameter is not straightforward. Li et al. (2019) have observed that the fractal exponent and Curie depth are so strongly inter-connected that they cannot be reliably estimated independently. In the de-fractal approach (e.g. Carrillo-de la Cruz et al., 2020a) the strategy is to choose the fractal parameter that gives the best fit between the observed and the modeled spectrum computed from the current estimation of the top and bottom of the magnetized layer (see Fig. 3c–e for example). Therefore, this approach is also subjective because of the broad minimum fitting errors that often occur by applying a range of fractal exponents and because of the correlation between the fractal parameter and the CPD that affects forward modeling (Li et al., 2019).

Generally speaking, the CPD estimations we have obtained using the de-fractal method (Fig. 5a) show similar patterns as using the centroid method (Fig. 5b), but the centroid method gives generally deeper CPD than the de-fractal method (see Figs. 3 and 5). The tendency of the de-fractal method to overcorrect the spectra and produce erroneously small Curie depths has been widely reported (Li et al., 2019; Kelemework et al., 2021). Therefore, the DBMS and CPD estimates using the de-fractal method can be considered to be biased to shallow depths at lower confidence than the centroid method estimates, in the context of a region dominated by cratonic crust but bordered by rifting.

3.5. Evaluation of the CPD errors

The errors of the centroid and top depths of the magnetic sources, ΔZ_0 and ΔZ_t, have been computed from the slope error of the linear fit (e.g., Ravat et al., 2007; Kelemework et al., 2021). Uncertainty of the depth to the bottom of the magnetic sources (ΔZ_b) has been computed using the standard propagation error formula (e.g. Martos et al., 2019):

$$\Delta Z_b = \sqrt{4\Delta Z_0^2 + \Delta Z_t^2} \quad (8)$$

The resulting statistical errors of the centroid and top depths of the magnetic sources have been found to be in the range of 0.24–1.05 and 0.01–0.34 km, respectively. The corresponding error of the DBMS, ΔZ_b, is in the range 0.5–2.1 km. This approach and similar magnitude errors have been obtained by many authors, e.g. 0.16–2.16 km in Coahuila, Mexico (Carrillo-de la Cruz et al., 2020a), less than 2 km beneath Thwaites Glacier in West Antarctica (Dziadek et al., 2021) and 0.53 km in Soutpansberg Basin, South Africa (Nyabeze and Gwavava, 2016). The same computations applied to the de-fractal method have yielded very similar results.

All the spectral methods and the estimates of fitting error have limitations that must be considered when interpreting the accuracy of the results with respect to both DBMS and CPD. Errors in choosing the

correct wavenumber band over which a linear fit is calculated may produce unpredictable errors that are very difficult to evaluate. Also, depth estimation is very sensitive to small variations of the fractal parameter. Moreover, depth estimations may be biased by sources at different depths which may affect the top depth estimations due to strong overlapping of the related spectral components (Hussein et al., 2013; Kelemework et al. (2021)). Uncertainties derived from these problems could be quantitatively estimated using Bayesian inversion (where parameters related to the thickness of magnetic sources are expressed in probability terms) because of its capability to incorporate prior information such as measurements from deep wells (Mather and Fullea, 2019; Audet and Gosselin, 2019; Lösing et al., 2020). However, the CPD uncertainty computed using the Bayesian approach requires very large window sizes 15-30 times larger than the deepest possible magnetic base in the study area (Mather and Fullea, 2019). Moreover, it is likely that factors other than curve fitting, like the separation of DBMS from CPD where deep lithology lacks magnetic sources (Kumar et al., 2021), cumulatively contribute greater uncertainty to the CPD estimate. Therefore, the errors in CPD are expected to be much greater than the estimated fitting errors and are likely to be of the order of many kilometers (e.g. Ravat et al., 2007; Mather and Fullea, 2019).

To address this uncertainty, the thermal gradient derived from the CPD estimates has been interpreted in the context of other data sets, including geothermal gradient and heat flux estimated from deep wells, resistivity distribution from magnetotelluric surveys, phase velocity variations from seismic tomography, tectonic setting of the regions and Moho elevations from seismic and gravity inversions.

3.6. Geothermal gradient and heat flow estimations

The estimated DBMS can be used to determine the temperature distribution at depths and consequently the geothermal gradient (Okubo et al., 1985). Firstly, we have assumed a proxy between the DBMS and CPD. The geothermal gradient $\left(\frac{\partial T}{\partial z}\right)$ has been calculated in each window as the ratio of the Curie temperature (T_c) of magnetite (580°C) in the crust and the estimated depth to the base of the magnetic source (DBMS) or Z_b assumed to be the Curie point depth (CPD) in each window.

$$\frac{\partial T}{\partial z} = \frac{\mathbf{T_c}}{\mathbf{Z_b}} \tag{9}$$

The surface heat flow $\mathbf{q_s}$ in each window is computed under the assumption that 1D steady-state conductive heat transfer dominates (e.g. Martos et al., 2017).

$$\mathbf{q_s} = \lambda \frac{\mathbf{T_c}}{\mathbf{Z_b}} \tag{10}$$

Where, λ is the average thermal conductivity coefficient of the rock. We choose to use an average thermal conductivity of 2.5 W/m°C because the basement rocks in Tanzania are dominantly the Precambrian gneiss, granulite and schist (Fritz et al., 2013, Fig. 1) with a conductivity range between 2 and 3 W/m°C (Ray et al., 2015).

3.7. Gravity data analysis

We have used gravity inversion to obtain Moho depth estimates over the large areas not covered by seismic data. The Moho depth estimates are used to compare the CPD and the associated geothermal gradients and heat flow derived from aeromagnetic data against crustal thickness. We use the new high resolution (5' x 5' arc minute) satellite-derived Free-Air gravity field model compilation SGG-UGM-2 (Liang et al., 2020) as our gravity data. In order to remove the gravity effect related to the topography we have computed the complete Bouguer anomaly using the ETOPO1 elevation map (Amante and Eakins, 2009), assuming Bouguer densities in the range 2.4 to 3 $\times$ 10^3 kg/m^3. As a final reference value, we have chosen 2.8 $\times$ 10^3 kg/m^3 because it showed the least correlation with the topography and is representative of the widespread exposure of crystalline rocks in the region.

The use of a Bouguer density of 2.8 $\times$ 10^3 kg/m^3 will overcorrect the gravity over areas where there is a significant thickness of sediments and/or water. We, therefore, have taken into account the density reductions due to water (in the lakes and the Indian Ocean) and sediments using the sediment thicknesses compilation from the CRUST1.0 Global model (Laske et al., 2013), verified against wells drilled to the basement along the coastal region of Tanzania (Didas, 2016). The densities of water and sediments were assumed to be 1, and 2.4 $\times$ 10^3 kg/m^3, respectively. Finally, we obtained the Bouguer anomaly compensated for water and sediments. To downweight the effects of the shallow intra-crustal density variations, we have applied a 150 km low pass filter.

The final gridded Bouguer anomaly (Fig. 4) indicates a broad zone of gravity low along the eastern rift axis and the surrounding area which extends south to the Archean Tanzanian craton. This anomaly is probably caused by a combination of features including the pre-existing thick crust caused by Precambrian tectonic collisions (Nyblade and Pollack, 1992), thickening of the crust due to Neoproterozoic collisional events during the formation of the Mozambique belt (Simiyu and Keller, 2001; Fritz et al., 2013), Cenozoic low density volcanoclastic rocks with thickness reaching 2 km on the rift flanks (Baker et al., 1988), crustal thickening due to intrusions near Moho (Hay et al., 1995) and the low density mantle beneath the apex of the Kenyan dome (Simiyu and Keller, 1997). The gravity low in the craton follows the trend of the area with Kimberlite pipes, indicating thick crust.

3.8. Estimation of Moho depth from gravity data

To infer the Moho depth distribution in Tanzania, we performed a constrained 3D inversion of the 150 km wavelength cut-off low pass filtered Bouguer gravity anomaly corrected for the sediments (Fig. 4). We used the GM-SYS 3D Geosoft Seequent software package. Forward modelling is based on a combination of Fast-Fourier Transform and space-domain algorithms to calculate the total response of the model (Parker, 1973). The inversion for solving the Moho depths is based on the procedure proposed by Parker and Huestis (1974) which assumes a simplified model of fixed densities of the crust and mantle. The algorithm solves iteratively for the thickness of a single layer representing the crust. This simplification in the model probably introduces the greatest departure from reality. The optimal solution is obtained when modeled Bouguer anomaly is close to the measured Bouguer anomaly within a given error. We assigned a constant density contrast of 0.5 $\times$ 10^3 kg/m^3 to the crust/mantle boundary, assuming average crustal and mantle densities of 2.8 and 3.3 $\times$ 10^3 kg/m^3, respectively. Since the inversion of gravity data is strongly affected by the non-uniqueness of the solutions, addition of *an a priori* constraint is needed to reduce the ambiguity (Kanda et al., 2019; Represas et al., 2012). As *an a priori* constraint, we have used the crustal thickness derived from seismic receiver functions compiled from several authors (Last et al., 1997; Dugda et al., 2005; Wölbern et al., 2010; Tugume et al., 2012; Kachingwe et al., 2015; Hodgson et al., 2017; Plasman et al., 2017; Borrego et al., 2018). The seismic receiver function crustal depth estimations have been gridded (Fig. 5d) to form a starting model for the gravity inversion and were used as a reference model during the inversion. The final crustal elevation model we have obtained is shown in Fig. 7 and described in paragraph 4.2. The final RMS error is 1.4 mGal. Finally, we have validated our results against the Global Moho depth by Laske et al. (2013). There is a good first-order match between our inversion and the global model over the areas covered by the receiver functions since our model has used receiver functions as constraints. In the large areas where receiver functions estimations from the global data set are not available, our model shows more detail. Note that the low pass filtering applied to the Bouguer gravity anomaly used for the

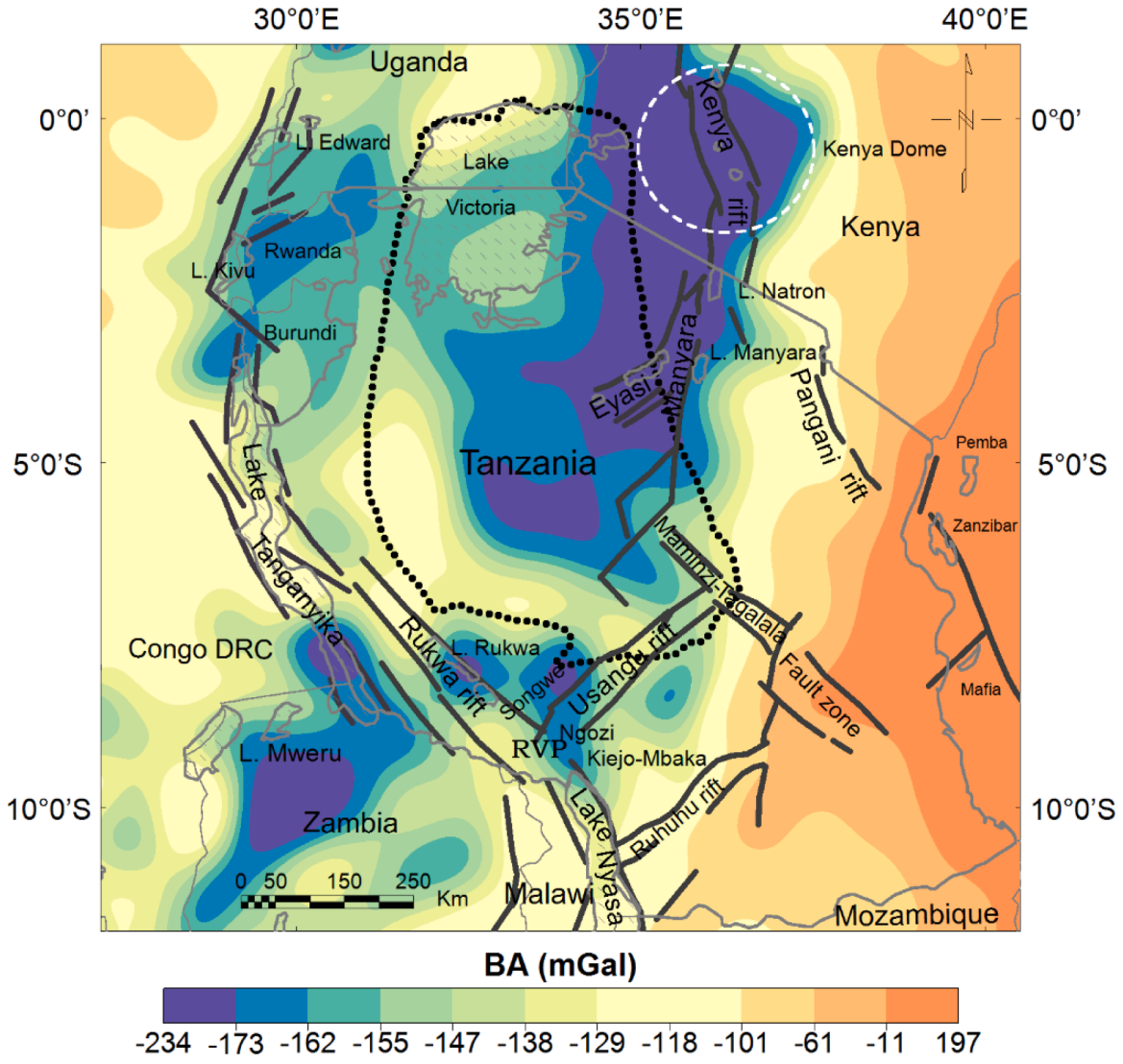

Fig. 4. The 150 km low pass filtered Bouguer gravity anomaly map, used here for the inversion. The dashed white ellipse indicates the Kenyan dome. The Tanzanian craton is outlined with a dotted black line. Thick black segment lines indicate the EARS.

inversion may have affected short-wavelength contributions from Moho, expected for instance along the rift axis.

4. Results

4.1. Curie point depth, geothermal gradient, heat flow and the geology of Tanzania

Overall results of the CPD, geothermal gradient and heat flow estimated from magnetic data are shown in Figs. 5 and 6. As a reference, in Fig. 5c we have reported the Global CPD estimated by Li et al. (2017). Our estimated CPDs range between 11 and 43 km beneath the geoid (Fig. 5a,b), the geothermal gradient ranges between 14 and 53 °C/km (Fig. 6a) while the heat flow values range between 34 and 132 mW/m^2 (Fig. 6b). As indicated in Fig. 5a,b, shallow CPDs are observed along the eastern branch of the EARS from Kenya through northern Tanzania where they terminate at the Eyasi rift as it diverges into the Archean Tanzanian craton (anomaly 2, Fig. 5a,b). In the western branch, shallow CPDs are seen southwest in the Rungwe volcanic province (RVP) and in the Rukwa rift. The northern part of the Malawi rift is characterized by shallow values of CPDs which increase partially to the south in Lake Nyasa. Other parts of the western rift valley associated with shallow CPDs are the central and southern parts of the Tanganyika rift basin and areas around Lake Kivu in Rwanda through northwest Burundi.

Apart from the EARS, shallow CPDs generally follow the Proterozoic continental-continental collision boundaries (anomalies 2, 3, 4, 5, 8 & 9) from the northeast through south: (i) at the Neoproterozoic collision boundaries between the Archean crust (Western Granulite) and the Neoproterozoic Mozambique belt (anomaly 2), (ii) along collision boundaries between the southern margin of the Archean Tanzanian craton and the Paleoproterozoic Usagaran-Ubendian belts (anomaly 4 & 5), (iii) at the collision boundary between Mesoproterozoic Irumide and Paleoproterozoic Usagaran belts (anomaly 8), (iv) at the collision boundary between the Irumide belt and Mozambique belt defined by the Ruhuhu and Kilombero rifts (anomaly 9). An unexpected pervasive zone of shallow CPDs in the Tanzanian craton (anomaly 1, Fig. 5a,b) is found south of Lake Victoria including the Ibadakuli geothermal site with the 65°C hot springs, where there is no surface expression of intense faulting related to the EARS. However, this anomaly is also observed in the global CPD (Fig. 5c, Li et al., 2017) and is related to a relatively shallow Moho depth (Fig. 5d) and the deeper low phase velocity from seismic tomography (Mulibo and Nyblade, 2013). The area is known for the world-class gold and diamond deposits hosted in meta-basalts and Cretaceous Kimberlites pipes, respectively. Geochemical studies of the hot springs indicate the absence of a shallow magmatic heat source and, therefore, they have been classified as being a result of a deep circulation

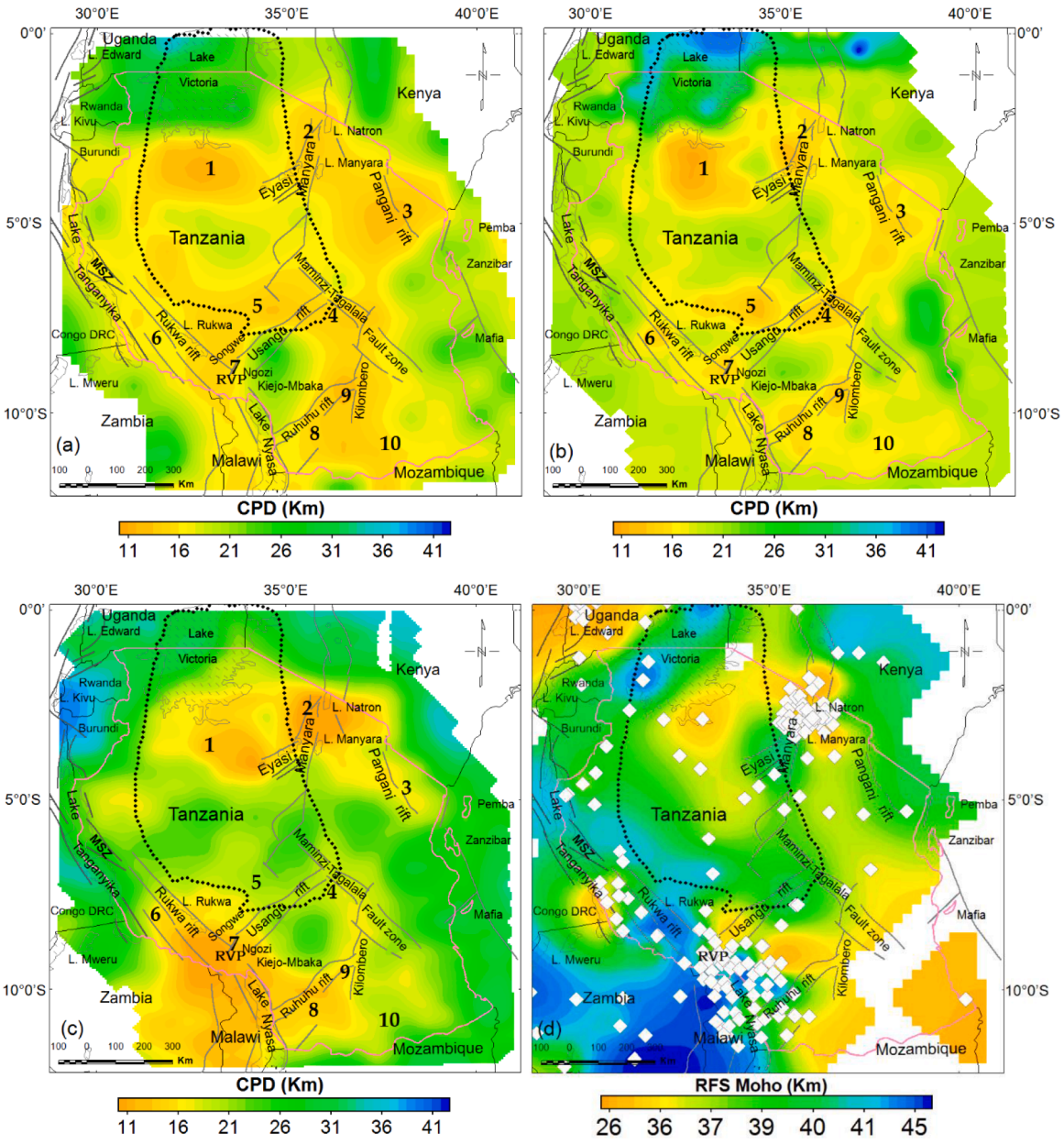

Fig. 5. Comparison of the CPD estimations from (a) Defractal method using 200 km widow sizes, (b) Centroid method using 110 km window sizes, (c) Global CPD map (Li et al., 2017), (d) Moho depth estimates from seismic receiver function used as constraints for 3D gravity inversion. Thick black segment lines indicate the extent of the EARS. White diamonds are the seismic stations. The numbers represent the heat flow anomalies discussed in chapter 5.

of a fault-controlled geothermal system (Hochstein et al., 2000; Hinz et al., 2018; TGDC, 2020) except the hot springs at the floor of the Ngozi caldera in the RVP which indicate magmatic affinity (Alexander et al., 2016).

The deepest CDP of 43 km in Tanzania is observed far away from the Proterozoic collision boundaries. High CPD values in nearby countries are observed in southeast Uganda and along the eastern shoulder of the rift in Kenya. A clear similarity between the CPD from this study in Fig. 5a and the Global CPD (Fig. 5c, Li et al., 2017) is observed but with additional information in the current results. Most of the low CPDs relate with zones under an extensional regime (Stamps et al., 2018) including anomalies 2, 3, 5, 6 and 7. A good correlation is also observed between the very low seismic phase velocity from seismic tomography (Mulibo and Nyblade, 2013) and the shallow CPD south of Lake Victoria and the associated high geothermal gradient and high heat flow.

4.2. Moho depths from 3D inversion of Bouguer gravity anomalies

The Moho depths based on a 3D inversion of Bouguer gravity data shown in Fig. 7 indicate a depth variation from 19 km offshore to 49 km beneath the Kenyan dome. From the Kenyan dome, large Moho depths extend to the south, following the western shoulder of the eastern rift into the Tanzanian craton. South of the craton, deep Moho is observed at the Proterozoic Ubendian-Usagaran mobile belts. From the offshore anomaly, the shallow Moho depth extends to the coastal area and southwards.

The localized shallow Moho expected beneath the eastern branch of the EARS based on seismic studies and magma encountered in geothermal wells in Menengai in the Kenyan rift (Mbia et al., 2015) is not resolved by the gravity inversion because of the filtering. However, zones of relatively shallow Moho depths of 36 km are observed to the north and south of the Kenyan dome while in the western branch

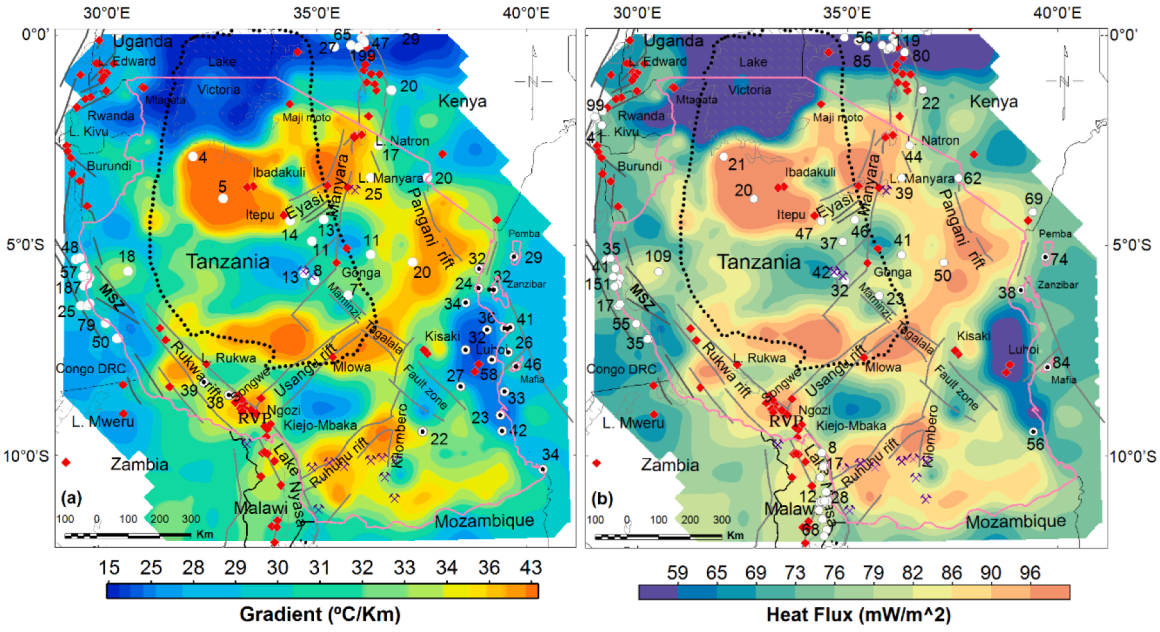

Fig. 6. Maps of estimated geothermal parameters from the radially averaged power spectrum of magnetic anomalies superimposed on structures. (a) Geothermal gradient map derived from Fig. 5a, (b) Heat flow map. White circles and white circles with a black dot are the shallow and deep hydrocarbon exploration wells, respectively. The numbers displayed are the numbers of available measured geothermal gradient or heat flow values from boreholes. The red diamonds are the hot springs and the crossed-pickaxe symbols indicate Uranium deposits. The maps are generated using minimum curvature gridding with a grid cell size of 2 km x 2 km.

shallow Moho depths are observed northwest and southeast of the Rukwa rift extending further south through western Malawi with an offset parallel to the rift axis. Below Lake Tanganyika, shallow Moho depths are revealed at the northern and central parts of the Lake. The Moho depths in the craton range from 45 km beneath the central part to 35 km in the southwest parallel to the northwest-trending Paleo-proterozoic Ubendian mobile belt. Localized zones with great Moho depths of 44 km are identified beneath the Ibadakuli, Maji-moto hot springs and below Lake Victoria.

5. Discussions

In order to better compare our results with existing information, we present several profiles across different geological and tectonic domains in Fig. 9. For each profile, we show in the upper panel the topography and the geological domains (see also Fig. 1). In the lower panel, we show our CPD estimates (magenta line), the global CPD estimation (blue) by Li et al. (2017), our gravimetric Moho (orange), the seismic Moho (green) from the global model of Laske et al. (2013) and the seismic Moho (black) from our compilation of existing receiver functions. Locations of the profiles are shown in Fig. 8. Profiles PL1 to PL4 are aligned EW in order to intersect the main structural features of the region and they include many locations of crustal thickness estimations derived from the seismic receiver functions (white diamonds). We have labelled the high heat flow anomalies 1 to 10 on the map and on the profiles. Below, we discuss each of these ten anomalies separately.

The Global CPD (Li et al., 2017) and the current CPD study are in fairly good agreement onshore, while offshore the global CPD is generally deeper in the mantle. We consider our estimation to be more reliable since it is based on the manual selection of frequency ranges to be linearly interpolated for each window while the procedure of Li et al. (2017) is necessarily automatic.

The gravity Moho is on average relatively deeper than the global seismic Moho. However, it is generally in good agreement with the receiver function Moho since the gravity Moho inversion has been constrained by the receiver function Moho. Both the gravimetric and global seismic crustal thickness estimations may be biased. Our gravimetric Moho depth estimation could be affected by density variations in the sediments and in the crust that have been assumed to be homogeneous. The seismic receiver function depth estimations may be affected by strong 3D effects and too short acquisition time.

5.1. Thermal structures beneath the Archean Tanzanian Craton

Overall, Archean cratons are known worldwide as the coolest landmasses on Earth associated with low heat production, low heat flow and low geothermal gradient compared to the surrounding Proterozoic mobile belts along which continental rifts subsequently develop (e.g., Lee and Uyeda, 1965; Lysak, 1987; Nyblade and Pollack, 1993). Therefore, deep CPD estimates and associated low heat flow values are expected beneath the craton lithosphere. Although Nyblade et al. (1990) have suggested that such a model generally applies to the Tanzanian Craton, our results indicate an unexpectedly high heat flow anomaly south of Lake Victoria and its southern region (anomaly 1, profiles P1, PL1 in Figs. 8 and 9). Our estimation is confirmed by the global CPD estimation by Li et al. (2017), unexpected shallow Moho estimations from seismic receiver function (Kachingwe et al., 2015) and low resistivity at a depth greater than 5 km (TGDC, 2020).

The rocks exposed in this area, including Meso-Archean meta-basalts (greenstone belts) and Neo-Archean Tonalite-trondhjemite-granodiorite (TTG) intrusions, are associated with a very shallow CPD of ~11 km and resulting high heat flow values of ~132 mW/m^2. The Ibadakuli geothermal site is in this area and is associated with hot springs with a maximum surface temperature discharge of 65°C. Two geothermal sites namely Itepu and Maji-moto are 120 km and 230 km to the southeast and northeast of this anomaly, respectively, with a surface temperature discharge of 60°C from a hot spring at the Maji-moto area (Hochstein et al., 2000). Seismological studies (e.g., Mulibo and Nyblade, 2013) demonstrate that the African mantle superplume which is responsible for the formation of the EARS is located below this heat flow anomaly. Once the plume reaches the base of the cratonic lithosphere, it forms two convective cells which spread to the east and west to open up the western and eastern branches of the EARS. Prior to the current plume activity, this area experienced widespread Kimberlite volcanism during Cretaceous to Tertiary times (Stiefenhofer and Farrow, 2004; Brown et al., 2012) indicating that this part of the craton was thermally

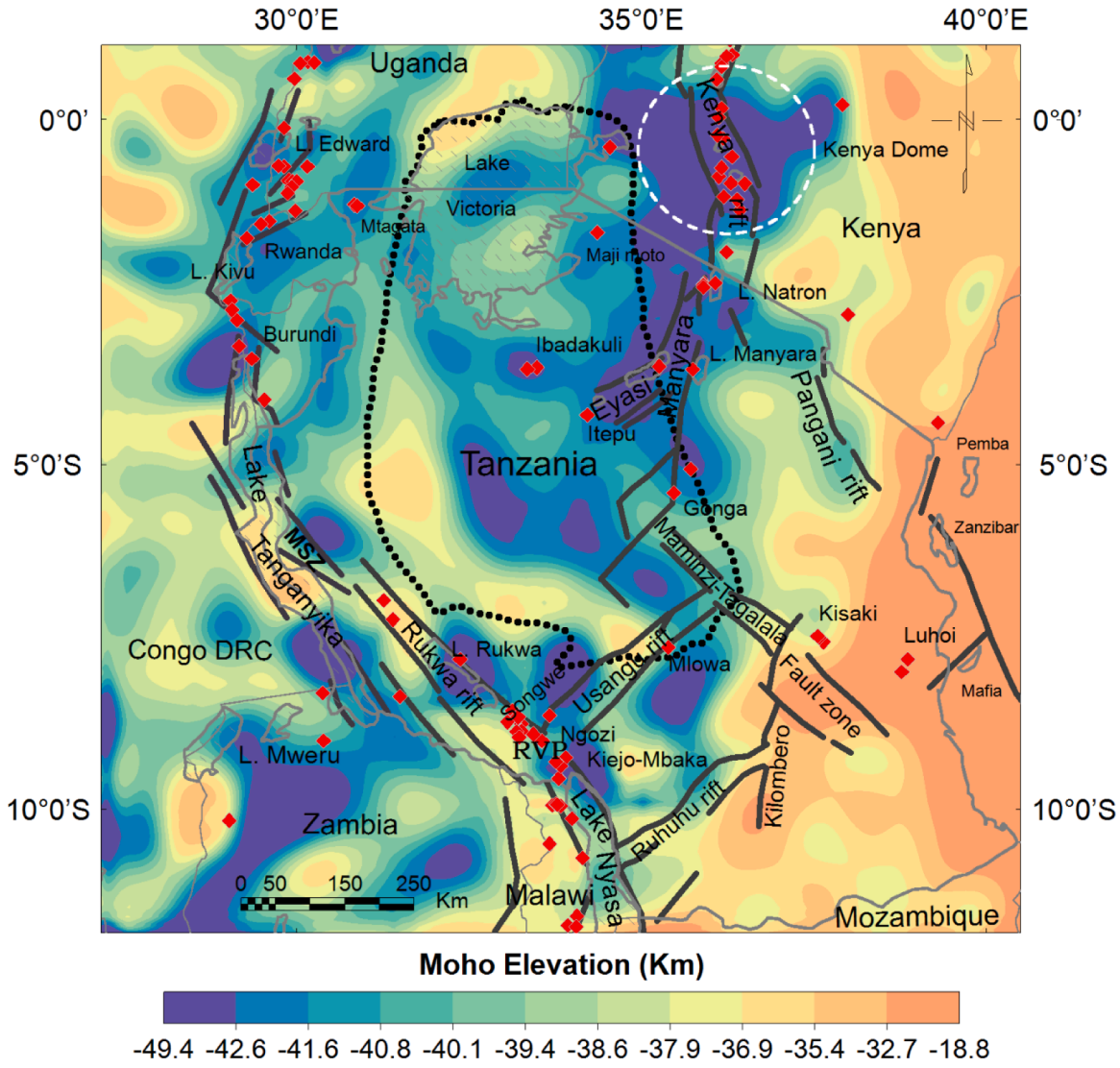

Fig. 7. Moho elevation map based on 3D inversion of Bouguer gravity data superimposed on hot spring locations (red diamonds). The main faults in the area are indicated by thick black lines. The black dotted polygon marks the boundary of the Archean Tanzanian craton. The stripped polygons are the lakes. The map is generated using the minimum curvature gridding with a grid cell size of 1 km × 1 km.

reactivated by the upwelling mantle superplume. The heat flow anomaly is associated with a relatively thin crust (see profiles P1 and PL1) of ~34 km from seismic studies (Kachingwe et al., 2015) that could be the result of intense heating caused by the hot mantle plume beneath the cratonic lithosphere as it extends towards the eastern and western branches of the EARS. Also, an abrupt decrease in average apparent resistivity from >1000 to about 100 Ωm at 1000 s period (corresponding to a depth of greater than 5 km) from magnetotelluric data at the Ibadakuli prospect (TGDC, 2020) may indicate a possible conductive anomaly at depth perhaps resulting from a high deep thermal gradient caused by the upwelling of the mantle superplume.

However, our estimated heat flow anomaly is not supported by the mean heat flow value of 34 ± 4 mW/m^2 as reported by Nyblade et al. (1990), Nyblade and Pollack (1993) and Nyblade (1997) and derived from shallow boreholes in the region (Fig. 6b). We suspect that the heat flow from shallow boreholes is not representative of the regional heat flow patterns, possibly because most of the boreholes were originally drilled for mineral exploration or groundwater consumption purposes. Therefore, the standard procedures for heat flow measurements have probably not been implemented. Temperature profiles of the boreholes also show borehole logs affected by cold-water inflow at a depth of 100–150 m (Nyblade, 1997), therefore, contributing to low surface heat flow. The other possible explanation is that the deep thermal perturbation associated with mantle superplume and rifting beneath the craton appears not yet to be conducted to the surface although it does along the rift axis.

We have also investigated the possibility that radiogenic heat production from granites rich U-Th-K could locally create significant heat. However, the two economically viable Uranium deposits in Manyoni district (Singida region) and Bahi district in Dodoma region (Kasoga et al., 2015) in the central part of the craton have no correlation with the location of the observed high heat flow values identified in this study, indicating low radiogenic heat contribution in the craton. Similarly, the high K (mean KO_2=4.95wt%) Archean granites in Mara region (area around the Maji-Moto hot spring) reported by Mshiu and Moboko (2012) do not correlate with high heat flow anomalies in this study. The lack of significant positive correlations between the areas with known radiogenic sources and heat flow zones suggests a minimum regional radiogenic heat contribution in the craton. However, at a local scale it may have a significant effect and, therefore, should not be completely ruled out. Gas geochemistry from Ibadakuli and the Maji-moto hot springs indicate the abundance of helium gas of continental origin

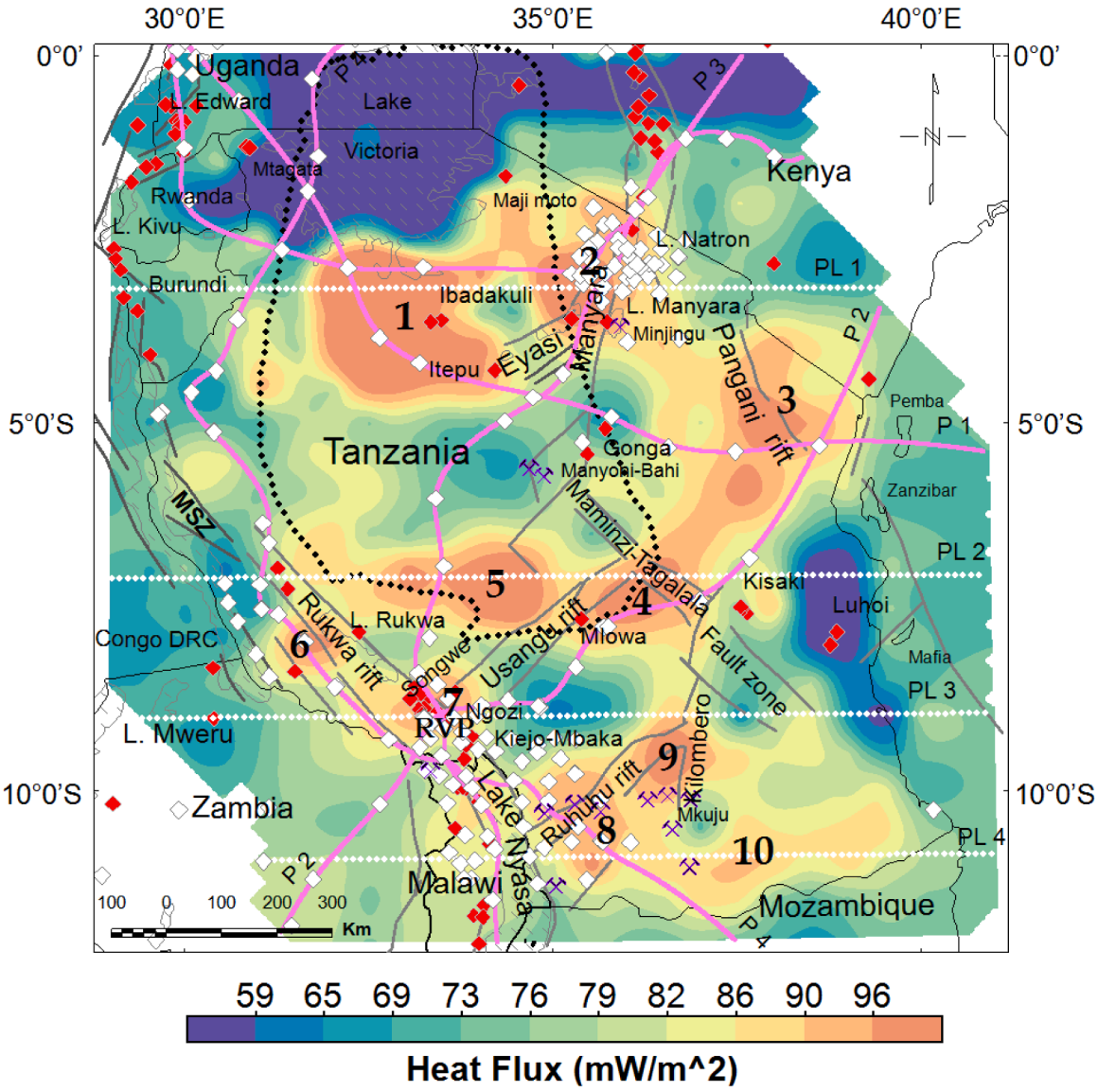

Fig. 8. Heat flow map superimposed on seismic stations (white diamonds), hot springs (red diamonds) and areas with Uranium deposits (crossed-pickaxe). The pervasive high heat flow zone south of Lake Victoria in the craton is very consistent with the Archean mid-oceanic ridge defined by the Mesoarchean greenstone belts (green polygons in Fig. 1) which were reactivated in Cretaceous by over 300 Kimberlite volcanisms and the uprising mantle superplume at the onset of the active EARS. The outline of the craton is marked with a black dotted polygon. The white dotted (PL) and pink coloured (P) lines are the selected profiles shown in Fig. 9. The numbers represent the heat flow anomalies discussed below.

accounting for about 36 mmol/mol and 13 % of the gas volume, respectively, derived from the decay of radiogenic elements in the crystalline basement of Archean crust (Hochstein et al., 2000; TGDC, 2020). Chandrasekhar et al. (2014) estimated the power capacity from these granites and assumed that each cubic kilometer of such granite has the capacity to generate about 42 × 10^{15} kWh of electricity with a temperature of 180°C at 5 km depth assuming the thermal gradient to be 40 °C/km and an average heat flow of 75 mW/m^2.

Although Kimberlite volcanism is usually associated with low crustal temperature, the large number of ~300 Kimberlite pipes present in the area may cause a significant thermal perturbation if heat is still preserved at depth. Hu et al. (2000) have suggested that residual heat flow may be preserved for millions of years after the ending of the deformation activity and is more dependent on the age of the last tectonothermal activity than the age of the province. Sclater et al. (1980) concluded that it takes about 800 Ma for the heat flow on the continents to decrease to the constant value of 46 mW/m^2. Therefore, based on our results, heat flow anomaly 1 is intruded by Kimberlites but also the small heat flow area to the south of anomaly 1 is intruded by a similar cluster of Kimberlite pipes. Therefore, the lack of consistency between the Kimberlites and the heat flow anomalies indicates the absence of direct heat contribution from the Cretaceous-Tertiary Kimberlite volcanism.

We, therefore, suggest that the thermal-mechanical instability in the craton was caused by the Cenozoic to present-day upwelling mantle superplume. It is likely that, due to the low permeability of the craton and the presence of shallow cold aquifers, the increase in deep heat flow interpreted beneath anomaly 1 is not widely manifested at the surface in the form of hot springs except at Ibadakuli area.

5.2. *Thermal structures beneath the Proterozoic mobile belts*

Generally speaking, the high heat flow anomalies follow the collision boundaries between the Paleo-Proterozoic Ubendian-Usagaran belt with the Archean Tanzanian craton to the south, and along a collision boundary between the Archean crust, also known as the western granulite (Fritz et al., 2013), with the Neoproterozoic Mozambique belt to

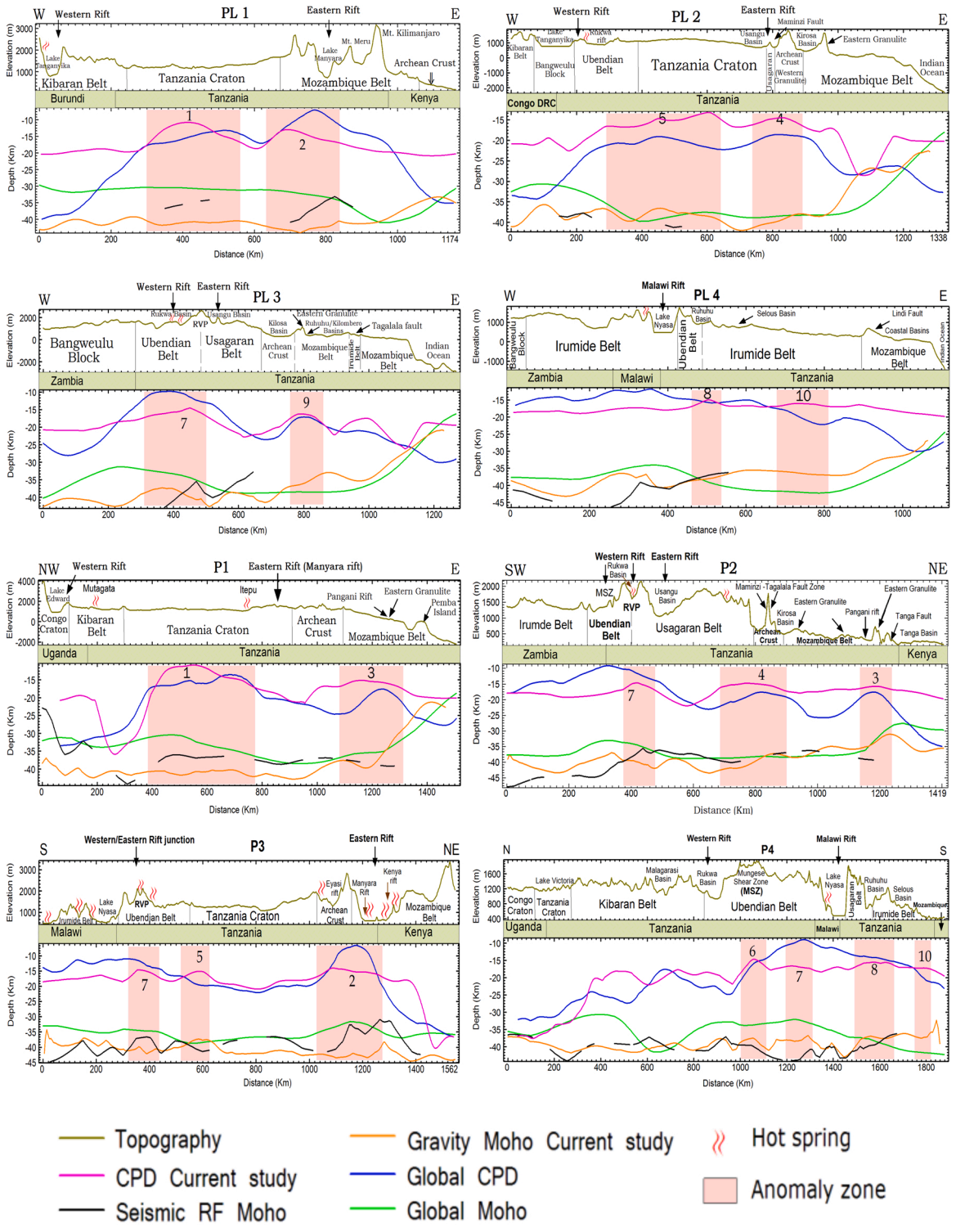

Fig. 9. Comparisons of the estimated CPD and gravity Moho with the global CPD (Li et al., 2017), global seismic Moho (Laske et al., 2013), seismic Moho from receiver functions and geological domains. The numbers are the locations of the high heat flow anomalies indicated in Fig. 8. Profile locations are shown in Figs. 1 and 8.

the east (Fig. 8). Moreover, high heat flow anomalies occur further south at the collision boundary between the Mesoproterozoic Irumide belt and the Neoproterozoic Mozambique belt. The heat flow is higher where the collision boundary is overprinted by the active EARS indicating thermal reactivation of the collision boundaries of the Proterozoic belts. These boundaries include: (i) Anomaly 2 (see profiles P3 and PL1), the area around the NTDZ which overprints the collision boundary between the Neoproterozoic Mozambique belt and the Archean western granulite. (ii) Anomaly 3 (profiles P1 and P2) along the Neoproterozoic Mozambique belt reactivated by the EARS which form the northwest-southeast Pangani rift. The elevated heat flow that demarcates the north, east and south boundaries of the Masai block is linked to the NTDZ, Pangani fault and the curving Neoproterozoic collision boundary, respectively, characterized by low density and low

seismic velocity (Ebinger et al., 2017; Tiberi et al., 2019). (iii) Anomaly 4 (profiles P2 and PL2) at the collision boundary between Paleoproterozoic Usagaran belt with the Archean craton overprinted by the south extension of the EARS (i.e., Maminzi fault and Usangu rift intersection zone). (iv) Anomaly 5 (profiles P3 and PL2) at the collision boundary between the Paleoproterozoic Ubendian belt with the Tanzanian craton overprinted by Kalema fault, the poorly developed eastern branch of the EARS. (v) Anomaly 6 (profile P4) at the collision boundary between the Ubendian and Bangweulu block marked by the Mungese shear zone. (vi) Anomaly 7 (profiles P2, P3, P4 and PL3) at the collision boundary between the Paleoproterozoic Usagaran-Ubendian belts overprinted by the east and west branches of the EARS at the Rungwe volcanic province. (vii) Anomaly 8 (profile P4 and PL4) at the collision boundary between the Paleoproterozoic Usagaran and Mesoproterozoic Irumide belts overprinted by the eastern branch of the EARS which form the Ruhuhu rift. (viii) Anomaly 9 at the collision boundary between the Neoproterozoic Mozambique belt and the Mesoproterozoic Irumide belt overprinted by the eastern branch of the EARS at the intersection between Kilombero and Ruhuhu basins which adjoins the central Malawi rift zone.

Our findings reveal that, besides the tectonic processes indicated by the seismic activity (O'Donnell et al., 2013), the Proterozoic sutures are affected by thermal processes, as indicated by the current shallower CPD, high heat flow and elevated geothermal gradient. The results also underlie the role played by the EARS in controlling tectonothermal processes at the Proterozoic collision boundaries.

5.3. Thermal structures beneath the Karoo Basins

High heat flow anomalies are present in the Permo-Triassic Karoo rift basins, particularly along the Ruhuhu-Kilombero Rift zone (anomaly 8 & 9, profiles P4 and PL3, PL4), and south of the Selous basin (anomaly 10, profile PL4) that is partially covered by the Karoo sediments. However, anomaly 9 appears to fit at the contact between the Paleoproterozoic Usagaran and Mesoproterozoic Irumide belts overprinted by the eastern branch of the EARS which Le Gall et al. (2004) suggest propagates through the Ruhuhu basin. Anomaly 8 is at the collision boundary between the Neoproterozoic Mozambique mobile belt and the Mesoproterozoic Irumide belt overprinted by the EARS in the Ruhuhu basin which adjoins the central Malawi rift. The huge Uranium deposit at Mkuju area in Selous basin, south Tanzania lies between anomaly 9 and 10. However, since these anomalies correspond to an updoming of the Moho elevation, we consider them to be a result of the mantle elevation rather than the radiogenic heat production from Uranium deposits. Moreover, there is no information about the existence of surface geothermal manifestations in this area with helium-rich hot springs which could be linked to radiogenic sources. Therefore, we interpret elevated heat flow values as being due to the recent reactivation by the EARS of the crustal extension and consequently elevated mantle associated with the Permo-Triassic rifting event. Crustal thickness studies from analysis of the seismic receiver function generally indicate that the Karoo Basins are characterized by a relatively thinner crust (30-38 km) compared to the thicker crust (46-50 km) in the surrounding area (Kachingwe et al., 2015; Borrego et al., 2018). This suggests that crustal thinning existed during Permo-Triassic rifting and is still preserved. A relatively high heat flow anomaly in Tanga (east of anomaly 3, profiles P1 and P2) is located at the intersection between Pangani and Tanga major faults probably reactivated by the EARS.

5.4. Thermal structures below Mesozoic sedimentary basins

In general, the southeast coastal sedimentary basins of Tanzania (Mandawa and Ruvuma basins) which form the passive continental margin are characterized by the lowest regional heat flow values (profiles PL2, PL3). The thick sedimentary cover of >4 km (Didas, 2016) should not affect the estimation of the bottom of the magnetic source and our low estimations are confirmed by the global estimation by Li et al. (2017). The progressive thinning of the crust towards the coast, imaged both by the seismic and gravimetric models has, therefore, been thermally compensated. Some known geothermal systems with shallow reservoirs (e.g. the Luhoi system along the Lindi fault zone) and the anomalously high bottom hole temperature of some deep oil wells have been explained as local anomalies formed by relatively deep hot fluid upwelling along faults (Armadillo et al., 2020).

However, the relatively high heat flow anomalies located offshore are probably caused by magmatic intrusions forming sills or dykes within the sedimentary section. Hot volcanic sill or dykes emplaced within Campanian sandstones were encountered in Mafia-1 well in Mafia island (Mpanda, 1997).

5.5. Thermal structures beneath the EARS

Our results indicate the highest heat flow of 90–104 mW/m^2 (anomaly 2) at the eastern branch of the EARS from the Manyara rift towards the south to the three rift segments of the NTDZ (see profile P3). The Kenyan rift would be expected to have the highest heat flow in East Africa. Therefore, the low heat flux, and moderate CPD in the eastern branch in Kenya is probably due to inadequate resolution caused by using a large data window size. A window size of 50 km × 50 km would resolve the anomaly below the Kenyan rift. Shallow CPD of 15 km has been estimated from magnetic data by Kuria et al. (2010) in the Olkaria geothermal field and validated using temperature logs from deep wells. Similarly, high heat flow is seen along the western branch at the southern triple junction in the Rungwe volcanic province (anomaly 7) where the eastern and western branches of the EARS converge (Fontijn et al., 2012). From this triple junction, the rift propagates to the south along the Malawi rift which is characterized by low to moderate heat flow. The high heat flow values in the EARS are due to the thinning of the crust and mantle elevation caused by the active crustal extension. This observation is supported by the minimum crustal thickness estimations along the rift axis from seismic receiver functions (Wölbern et al., 2010; Tugume et al., 2012; Laske et al., 2013; Hodgson et al., 2017; Plasman et al., 2017; Borrego et al., 2018), shallow low seismic velocity zone (Mulibo and Nyblade, 2013; Ebinger et al., 2017; Grijalva et al., 2018; Tiberi et al., 2019) and low-density zone (Tiberi et al., 2019).

The Ngozi geothermal area located at the southern triple junction (in the Rungwe volcanic province) where the eastern and western branches of the EARS intersect, is characterized by high heat flow values of ~98 mW/m^2. Na-K geothermometry from the hot springs (66–89°C) indicated a high temperature geothermal system with a reservoir temperature greater than 230°C heated by a magmatic body located within a depth range of 5–7 km below the Ngozi caldera (Alexander et al., 2016; Didas and Hersir, 2020). The Ngozi area is bordered by some geothermal systems characterized by a lack of apparent magmatic contribution to the water and gas chemistry, including the 140°C reservoir in the Kiejo-Mbaka prospect located about 50 km to the southeast (Rizzello et al., 2018) and the 120°C reservoir in the Songwe prospect (Alexander et al., 2016) located about 50 km northwest. Further south of the Ngozi prospect, the Malawi rift is characterized by numerous hot springs with measured temperatures of up to 80°C aligned with the rift margin (e.g., Njinju et al., 2019). At a regional scale, the Ngozi and Songwe prospects are linked to the same heat flow anomaly with the peak located at the Ngozi-Rungwe volcanoes, while the Kiejo-Mbaka prospect seems to form an independent system. In fact, it is considered to be an extensional domain play fault-controlled system with lateral leakage (Rizzello et al., 2018).

Unlike the magma-rich eastern branch of the EARS (Foster et al., 1997) associated with numerous fumaroles and hot springs and the poorly magmatic Malawi rift (Ebinger et al., 2019), associated with many hot springs, the poorly magmatic Lake Tanganyika rift has very few surface geothermal manifestations (ARGeo, 2021) and is generally

characterized by relatively elevated but discontinuous heat flow zones (anomalies to the west and further northwest of anomaly 6, respectively). The central heat flow anomaly (northwest of anomaly 6) is the largest and corresponds to the contact between the Paleoproterozoic Ubendian and Mesoproterozoic Kibaran mobile belts which is reactivated by the EARS by the Mungese shear zone which extends southeast in the Rukwa rift. The highest heat flow values of 154 mW/m^2, measured from shallow boreholes drilled at the bottom of Lake Tanganyika, are within this anomaly and confirm our estimations. Along the Malawi rift, our results indicate a region of relatively high heat flow at the northern part of Lake Nyasa corresponding to the hot springs and uniform distribution of relatively deep CPDs in the central part associated with low heat flow. According to Njinju et al., 2019, the regions of highest heat flow (70-82 mW/m^2) in the Malawi rift zone are concentrated within the Permo-Triassic Karroo rift basins that, in Tanzania, correspond to anomaly 8 and 9 which lie along the Ruhuhu basin at the Proterozoic collision boundaries, as already mentioned.

The low heat flow between anomalies 2 and 3, associated with the dormant volcanoes, Mt. Kilimanjaro and Mt. Meru in northeast Tanzania, may be a computational artefact related to the resolution in the data window that includes the volcanoes and the surrounding areas and/or it may be related to extensive alteration of the rocks that eliminated magnetic minerals. Neither the Kilimanjaro nor Meru volcanoes demonstrate shallow CPD or elevated thermal anomalies (e.g., profile PL 1 in Fig. 9) and there are no surface geothermal manifestations other than the volcanoes itself. The question is whether the surrounding lithosphere is thick and cold, or if the volcanoes are associated with localized deep structures enhancing the rise of local plumes. The former is supported by the large crustal thickness based on seismic receiver function analysis. Thick crust between 37 and 40 km is common beneath the areas surrounding the volcanoes compared to the relatively thinner crust between 29 and 32 km along the rift axis (Last et al., 1997; Dugda et al., 2005; Plasman et al., 2017).

6. Conclusion

We have used the inversion of the radially averaged power spectra of the magnetic anomalies to estimate the Curie point depth of the magnetic sources, geothermal gradient and surface heat flow in Tanzania. We found that the high heat flow anomalies often correspond to shallow Moho and are generally found where the Proterozoic collision boundaries underwent tectonic and thermal reactivation by the EARS.

High heat flow is observed along the EARS at the north Tanzania divergence zone (NTDZ) of the eastern branch, while in the western branch it is observed in the Rukwa rift and at the Rungwe Volcanic Province (RVP) located at the triple junction of the eastern and western branches of the EARS and Malawi rift. The high heat flow values in the RVP and in the NTDZ are due to Cenozoic magmatism in the EARS which is caused by thinning of the crust and mantle elevation as a result of crustal extension.

The unexpectedly wide zone of high heat flow to the south of Lake Victoria in the Archean craton is associated with the African mantle superplume which originates from the mantle-core boundary to the base of the craton where it forms two convective cells that drive the opening of the eastern and western branches of the EARS. Radiogenic heat production from Uranium deposits and K-rich granites in the area do not appear to contribute significantly to the regional heat flow. Low heat flow values are seen in the central part of the Archean craton and away from the suture zones of the Proterozoic mobile belts.

Our findings have revealed unexplored geothermal potentials along i) the Proterozoic collision boundaries reactivated by the EARS, ii) the RVP and iii) NTDZ.

CRediT authorship contribution statement

Makoye Mabula Didas: Conceptualization, Methodology, Software, Formal analysis, Writing – original draft, Writing – review & editing. **Egidio Armadillo:** Conceptualization, Methodology, Data curation, Resources, Writing – review & editing. **Gylfi Páll Hersir:** Funding acquisition, Project administration, Writing – review & editing, Supervision, Resources, Conceptualization. **William Cumming:** Resources, Writing – review & editing, Supervision, Conceptualization. **Daniele Rizzello:** Supervision, Writing – review & editing.

Declaration of Competing Interest

The authors declare that they have no known competing financial interests or personal relationships that could have appeared to influence the work reported in this paper.

Acknowledgments

This research was financially supported by the GRÓ Geothermal Training Programme in Iceland (GRÓ GTP) under the auspices of UNESCO (formerly UNU-GTP). It is a part of the PhD programme of the first author carried out at the University of Iceland. Their support is greatly acknowledged. The aeromagnetic data were provided by the Geological Survey of Tanzania (GST) in collaboration with the Tanzania Geothermal Development Company (TGDC) as a part of the geothermal exploration database in Tanzania. The public data, Global CPD are from https://www.nature.com a product work by Li et al. (2017), SRTM-DEM data are the product of USGS available at https://lpdaac.usgs.gov and the Crustal thickness from https://igppweb.ucsd.edu/~gabi/crust1.html the product of Laske et al. (2013). The Tanzania Geothermal Development Company (TGDC) is thanked for its continuous support in facilitating this work as well as the PhD study of the first author. We thank Juan Luis Carrillo-de la Cruz for providing MAGCPD software used for CPD estimations. We are thankful to PhD committee members, Ásdís Benediktsdóttir and Halldór Geirsson for useful discussions, insights and reviews during this study. Finally, Dr. Craig Miller is acknowledged for his careful review of the manuscript; constructive and most useful comments.

References

Alexander, K., Cumming, W.B., Malini, L., 2016. Technical review of geothermal potential of ngozi and songwe geothermal prospects. In: Proceedings of the 6th African Rift Geothermal Conference. Addis Ababa, Ethiopia.

Andrés, J., Marzán, I., Ayarza, P., Martí, D., Palomeras, I., Torné, M., Campbell, S., Carbonell, R., 2018. Curie point depth of the Iberian Peninsula and surrounding margins. A thermal and tectonic perspective of its evolution. J. Geophys. Res. Solid Earth 123, 2049–2068. https://doi.org/10.1002/2017JB014994.

Armadillo, E., Rizzello, D., Pasqua, C., Pisani, P., Ghirotto, A., Didas, M., et al., 2020. Geophysical constraints on the Luhoi (Tanzania) geothermal conceptual model. Geothermics 87, 101875. https://doi.org/10.1016/j.geothermics.2020.101875.

Asefa, J., Ayele, A., 2020. Complex tectonic deformation in circum-Tanzania craton: East African rift system. J. Afr. Earth Sci. 170, 103893 https://doi.org/10.1016/j.jafrearsci.2020.103893.

Audet, P., Gosselin, M.J., 2019. Curie depth estimation from magnetic anomaly data: are-assessment using multitaper spectral analysis and Bayesian inference. Geophys. J. Int. 218, 494–507. https://doi.org/10.1093/gji/ggz166.

Baker, B.H., Mitchell, J.G., Williams, L.A.J., 1988. Stratigraphy, geochronology and volcano-tectonic evolution of the Kedong-Naivasha-Kinangop region, Gregory rift valley, Kenya. J. Geol. Soc. Lond. 145, 107–116. https://doi.org/10.1144/gsjgs.145.1.0107.

Bansal, A.R., Dimri, V.P., 1999. Gravity evidence for mid crustal domal structure below Delhi fold belt and Bhilwara super group of western India. Geophys. Res. Letters 26, 2793–2795. https://doi.org/10.1029/1999GL005359.

Bansal, A.R., Dimri, V.P., 2001. Depth estimation from the scaling power spectral density of nonstationary gravity profile. Pure Appl. Geophys. 158, 799–812. https://doi.org/10.1007/PL00001204.

Bansal, A.R., Dimri, V.P., 2005. Depth determination from nonstationary magnetic profile for scaling geology. Geophys. Prospect. 53, 399–410. https://doi.org/10.1111/j.1365-2478.2005.00480.x.

Bansal, A.R., Dimri, V.P., Sagar, G.V., 2006. Depth estimation from gravity data using the maximum entropy method (MEM) and multi taper method (MTM). Pure Appl. Geophys. 163, 1417–1434. https://doi.org/10.1007/s00024-006-0080-8.

Bansal, A.R., Gabriel, G., Dimri, V.P., 2010. Power law distribution of susceptibility and density and its relation to seismic properties: an example from the German

continental deep drilling program. J. Appl. Geophys. 72, 123–128. https://doi.org/10.1016/j.jappgeo.2010.08.001.
Bansal, A.R., Gabriel, G., Dimri, V.P., Krawczyk, C.M., 2011. Estimation of the depth to the bottom of magnetic sources by a modified centroid method for fractal distribution of sources: an application to aeromagnetic data in Germany. Geophysics 76, 11–22. https://doi.org/10.1190/1.3560017.
Bhattacharya, B.K., Leu, L.K., 1975. Analysis of magnetic anomalies over yellowstone national park: mapping of curie point isothermal surface for geothermal reconnaissance. J. Geophys. Res. 80, 4461–4465. https://doi.org/10.1029/JB080i032p04461.
Blakely, R.J., 1995. Potential Theory in Gravity & Magnetic Applications. Cambridge Univ. Press.
Bouligand, C., Glen, J.M.G., Blakely, R.J., 2009. Mapping Curie temperature depth in the western United States with a fractal model for crustal magnetization. J. Geophys. Res. 114, B11104. https://doi.org/10.1029/2009JB006494.
Boniface, N., Appel, P., 2017. Stenian - Tonian and Ediacaran metamorphic imprints in the southern Paleoproterozoic Ubendian Belt, Tanzania: constraints from *in situ* monazite ages. J. Afr. Earth Sci. 133, 25–35. https://doi.org/10.1016/j.jafrearsci.2017.05.005.
Boniface, N., Schenk, V., Appel, P., 2012. Paleoproterozoic eclogites of MORBtype chemistry and three Proterozoic orogenic cycles in the Ubendian belt (Tanzania): evidence from monazite and zircon geochronology, and geochemistry. Precambrian Res. 192-195, 16–33. https://doi.org/10.1016/j.precamres.2011.10.007.
Boniface, N., 2019. An overview of the Ediacaran-Cambrian orogenic events at the southern margins of the Tanzania craton: implication for the final assembly of Gondwana. J. Afr. Earth Sci. 150, 123–130. https://doi.org/10.1016/j.jafrearsci.2018.10.015.
Borg, G., Krogh, T., 1999. Isotopic age data of single zircons from the Archean Sukumaland greenstone belt, Tanzania. J. Afr. Earth Sci. 29, 301–312. https://doi.org/10.1016/S0899-5362(99)00099-8.
Borrego, D., Nyblade, A.A., Accardo, N.J., Gaherty, J.B., Ebinger, C.J., Shillington, D.J., et al., 2018. Crustal structure surrounding the northern Malawi rift and beneath the Rungwe Volcanic Province, East Africa. Geophys. J. Int. 215, 1410–1426. https://doi.org/10.1093/gji/ggy331.
Brown, R.J., Manya, S., Buisman, I., Fontana, G., Field, M., Mac Niocaill, C., Stuart, F.M., 2012. Eruption of Kimberlite magmas: physical volcanology, geomorphology and age of the youngest kimberlitic volcanoes known on earth (the upper Pleistocene/Holocene Igwisi Hills volcanoes, Tanzania). Bull. Volcanol. 74 (7), 1621–1643. https://doi.org/10.1007/s00445-012-0619-8.
Bumby, A.J., Guiraud, R., 2005. The geodynamic setting of the Phanerozoic basins of Africa. J. Afr. Earth Sci. 43, 1–12. https://doi.org/10.1016/j.jafrearsci.2005.07.016.
Bussert, R., Heinrich, W.D., Aberhan, M., 2009. The Tendaguru formation (late Jurassic to early cretaceous, Southern Tanzania): definition, palaeoenvironments, and sequence stratigraphy. Foss. Rec. 12, 141–174. https://doi.org/10.1002/mmng.200900004.
Carrillo-de la Cruz, J.L., Prol-Ledesma, R.M., Gomez-Rodríguez, D., Rodríguez-Díaz, A. A., 2020a. Analysis of the relation between bottom hole temperature data and Curie temperature depth to calculate geothermal gradient and heat flow in Coahuila. Mexico. Tectonophysics 780, 228397. https://doi.org/10.1016/j.tecto.2020.228397.
Carrillo-de la Cruz, J.L., Prol-Ledesma, R.M., Vel´azquez-Sanchez, P., Gomez-Rodríguez, D., 2020b. MAGCPD: a MATLAB-based GUI to calculate the Curie point-depth involving the spectral analysis of aeromagnetic data. Earth Sci. Inf. 13, 1539–1550. https://doi.org/10.1007/s12145-020-00525-x.
Carrillo-de la Cruz, J.L., Prol-Ledesma, M.R., Gabriel, G., 2021. Geostatistical mapping of the depth to the bottom of magnetic sources and heat flow estimations in Mexico. Geothermics 97, 102225. https://doi.org/10.1016/j.geothermics.2021.102225.
Chandrasekhar, V., Omenda, P., Chandrasekharam, D., 2014. High heat generating granites of Tanzania. In: Proceedings of the 5th African Rift Geothermal Conference Arusha. Tanzania.
Chiozzi, P., Matsushima, J., Okubo, Y., Pasquale, V., Verdoya, M., 2005. Curie-point depth from spectral analysis of magnetic data in Central–Southern Europe. Phys. Earth Planet. Inter. 152 (4), 267–276. https://doi.org/10.1016/j.pepi.2005.04.005.
Didas, M.M, 2016. Geophysical Investigation of the Subsurface Structures of the Mandawa basin, Southeast Coastal Tanzania. University of Dar es Salaam, p. 170. MSc. Thesis (unpublished.
Didas, M.M., Hersir, G.P., 2020. 1D joint inversion of MT and TEM data from Ngozi geothermal prospect, southwest Tanzania. An integrated interpretation of geoscientific results. In: Proceedings of the World Geothermal Congress 2020+1. Reykjavik, Iceland.
Dimri, V.P., Dimri, V.P., 2000. Crustal fractal magnetization. Application of Fractals in Earth Sciences. A. A. Balkema/Oxford and IBH Publishing Co., pp. 89–95. ISBN 9789054102847.
Dimri, V.P., Bansal, A.R., Srivastava, R.P., Vedanti, N., Mahadevan, T.M., Arora, B.R., Gupta, K.R., 2003. Scaling behaviour of real earth source distribution: Indian case studies. Indian Continental Lithosphere: Emerging Research Trends. Geological Society India Memoir, pp. 431–448, 53.
Dolmaz, M.N., Ustaomer, T., Hisarli, Z.M., Orbay, N., 2005. Curie point depth variations to infer thermal structure of the crust at the African-Eurasian convergence zone, SW Turkey. Earth Planets Space 57, 373–383. https://doi.org/10.1186/BF03351821.
Dugda, M.T., Nyblade, A.A., Julia, J., Langston, C.A., Ammon, C.J., Simiyu, S., 2005. Crustal structure in Ethiopia and Kenya from receiver function analysis: implications for rift development in eastern Africa. J. Geophys. Res. 110, (B)01303. https://doi.org/10.1029/2004JB003065, 2005.
Dziadek, R., Ferraccioli, F., Gohl, K., 2021. High geothermal heat flow beneath Thwaites Glacier in West Antarctica inferred from aeromagnetic data. Commun. Earth Environ. https://doi.org/10.1038/s43247-021-00242-3.
Ebinger, C.J., Poudjom, Y., Mbede, E., Foster, F., Dawson, J., 1997. Rifting archean lithosphere: the Eyasi–Manyara–Natron rifts, East Africa. J. Geol. Soc. Lond. 154, 947–960. https://doi.org/10.1144/gsjgs.154.6.0947.
Ebinger, C., 1989. Tectonic development of the western branch of the East Africa rift system. Bull. Seismol. Soc. Am. 101, 885–903. https://doi.org/10.1130/0016-7606(1989)101<0885:TDOTWB>2.3.CO;2.
Ebinger, C.J., Oliva, S.J., Pham, T.-Q., Peterson, K., Chindandali, P., Illsley-Kemp, F., et al., 2019. Kinematics of active deformation in the Malawi rift and Rungwe Volcanic Province, Africa. Geochem. Geophys. Geosyst. 20, 3928–3951. https://doi.org/10.1029/2019GC008354.
Ebinger, C.J., Keir, D., Bastow, I.D., Whaler, K., Hammond, J.O.S., Ayele, A., Hautot, S., 2017. Crustal structure of active deformation zones in Africa: implications for global crustal processes. Tectonics 36, 3298–3332. https://doi.org/10.1002/2017TC004526.
Fadaie, K., Ranalli, G., 1990. Rheology of the lithosphere in the East African rift system. Geophys. J. Int. 102, 445–453. https://doi.org/10.1111/j.1365-246X.1990.tb04476.x.
Fontijn, K., Williamson, D., Mbede, E., Ernst, G.G.J., 2012. The Rungwe volcanic province, Tanzania-a review. J. Afr. Earth Sci. 63, 12–31. https://doi.org/10.1016/j.jafrearsci.2011.11.005.
Foster, A., Ebinger, C., Mbede, E., Rex, D., 1997. Tectonic development of the northern Tanzania sector of the East African rift system. J. Geol. Soc. Lond. 154, 689–700. https://doi.org/10.1144/gsjgs.154.4.0689.
Fritz, H., Abdelsalam, M., Ali, K., Bingen, B., Collins, A., Fowler, A., et al., 2013. Orogen styles in the East African orogen: a review of the Neoproterozoic to Cambrian tectonic evolution. J. Afr. Earth Sci. 86, 65–106. https://doi.org/10.1016/j.jafrearsci.2013.06.004.
Grijalva, A., Nyblade, A.A., Homman, K., Accard, N.J., Gaherty, J.B., Ebinger, C.J., Mulibo, G., 2018. Seismic evidence for plume-and craton-influenced upper mantle structure beneath the Northern Malawi rift and the Rungwe Volcanic Province, East Africa. Geochem. Geophys. Geosyst. 19 (10), 3980–3994. https://doi.org/10.1029/2018GC007730.
Hay, D.E., Wendlandt, R.F., Keller, G.R., 1995. The origin of Kenya rift plateau-type flood phonolites: integrated petrologic and geophysical constraints on the evolution of the crust and upper mantle beneath the Kenya rift. J. Geophys. Res. 100, 5435–5444. https://doi.org/10.1029/94JB03036.
ARGeo. (n.d.). Home, 2021. ARGeo AGID Database August 2021. https://agid.theargeo.org/.
Hersir, G.P., Kristinsson, S.G., Mnjokava, T., 2015. Tanzania Visit in January 2015. Assessment of Areas for Surface Exploration Studies and Training Needs. Internal Report Prepared for TGDC with Funding from ICEIDA. Iceland GeoSurvey, Report number ÍSOR-2015/025. 48pp.
Hinz, N., Cumming, W.B., Sussman, D., 2018. Exploration of fault-related deep-circulation geothermal resources in the western branch of the East African rift system: examples from Uganda and Tanzania. In: Proceedings of the 7th African Rift Geothermal Conference. Kigali, Rwanda.
Hochstein, M.P., Temu, E.B., Moshy, C.M.A, 2000. Geothermal resources of Tanzania. In: Proceedings of the World Geothermal Congress. Kyushu-Tohoku, Japan.
Hodgson, I., Illsley-Kemp, F., Gallacher, R.J., Keir, D., Ebinger, C.J., Mtelela, K., 2017. Crustal structure at a young continental rift: a receiver function study from the Tanganyika Rift. Tectonics 36 (12), 2806–2822. https://doi.org/10.1002/2017TC004477.
Hu, S., He, L., Wang, J., 2000. Heat flow in the continental area of China: a new data set. Earth Planet. Sci. Lett. 179 (2), 407–419. https://doi.org/10.1016/S0012-821X(00)00126-6.
Hunt, C.P., Moskowitz, B.M., Banerjee, S.K., 1995. Magnetic properties of rocks and minerals. Rock Physics & Phase Relations: A Handbook of Physical Constants, vol. 3. T. J. Ahrens, Ed., Washington, DC, USA: AGU Ref. Shelf, pp. 189–204. https://doi.org/10.1029/RF003p0189.
Hussein, M., Mickus, K., Serpa, L.F., 2013. Curie point depth estimates from aeromagnetic data from death valley and surrounding regions, California. Pure Appl. Geophys. 170 (4), 617–632. https://doi.org/10.1007/s00024-012-0557-6.
Kabaka, K.T., Mnjokava, T.T., Kajugus, S.I., 2016. Geothermal development in Tanzania, a country update. In: Proceedings of the 6th African Rift Geothermal Conference. Addis Ababa, Ethiopia.
Kabete, J.M., Groves, D.I., McNaughton, N.J., Mruma, A.H., 2012a. A new tectonic and temporal framework for the Tanzanian shield: implications for gold metallogeny and undiscovered endowment. Ore Geol. Rev. 48, 88–124. https://doi.org/10.1016/j.oregeorev.2012.02.009.
Kabete, J.M., McNaughton, N.J., Groves, D.I., Mruma, A.H., 2012b. Reconnaissance SHRIMP U–Pb zircon geochronology of the Tanzania craton: evidence for Neoarchean granitoid–greenstone belts in the central Tanzania region and the Southern East African Orogen. Precambrian Res. 216–219, 232–266. https://doi.org/10.1016/j.precamres.2012.06.020.
Kachingwe, M., Nyblade, A., Julia, J., 2015. Crustal structure of precambrian terranes in the southern African subcontinent with implications for secular variation in crustal genesis. Geophys. J. Int. 202, 533–547. https://doi.org/10.1093/gji/ggv136.
Kagya, M.L., 1996. Geochemical characterization of Triassic petroleum source rock in the Mandawa basin, Tanzania. J. Afr. Earth Sci. 23, 73–88. https://doi.org/10.1016/S0899-5362(96)00053-X.
Kalberkamp, U., Schaumann, G., Ndonde, P.B., Chiragwile, S.A., Mwano, J.M, GEOTHERM Working Group, 2010. Surface exploration of a viable geothermal

resource in Mbeya area, SW Tanzania. In: Part III: Geophysics. Proceedings of the World Geothermal Congress 2010. Bali, Indonesia.
Kanda, I., Fujimitsu, Y., Nishijima, J., 2019. Geological structures controlling the placement and geometry of heat sources within the Menengai geothermal field, Kenya as evidenced by gravity study. Geothermics 79, 67–81. https://doi.org/10.1016/j.geothermics.2018.12.012.
Kasoga, K.F., Mwalongo, D.A., Sawe, S.F., Nyaruba, M.M., Dammalapati, U., 2015. Ambient gamma dose rate measurements at Manyoni uranium deposits, Singida, Tanzania. In: Proceedings of SAIP2015. ISBN: 978-0-620-70714-5.
Kelemework, Y., Fedi, M., Milano, M., 2021. A review of spectral analysis of magnetic data for depth estimation. Geophysics 86 (6), J33. https://doi.org/10.1190/geo2020-0268.1.
Kent, P.E., Hunt, J.A., Johnstone, D.W., 1971. The Geology and Geophysics of Coastal Tanzania. Her Majesty's Stationary Office (HMSO), London. Geophysical Paper N. 6. ISBN 0118801384.
Kröner, A., Muhongo, S., Hegner, E., Wingate, M., 2003. Single-zircon geochronology and Nd isotopic systematics of Proterozoic high-grade rocks from the Mozambique Belt of southern Tanzania (Masasi area): implications for Gondwana assembly. J. Geol. Soc. 160, 745–757. https://doi.org/10.1144/0016-764901-170.
Kumar, R., Bansal, A.R., Ghods, A., 2020. Estimation of depth to bottom of magnetic sources using spectral methods: application on Iran's aeromagnetic data. J. Geophys. Res. Solid Earth 125 (3). https://doi.org/10.1029/2019JB018119.
Kumar, R., Bansal, A.R., Betts, P.G., Ravat, D., 2021. Re-assessment of the depth to the base of magnetic sources (DBMS) in Australia from aeromagnetic data using the defractal method. Geophys. J. Int. 225, 530–547. https://doi.org/10.1093/gji/ggaa601.
Kuria, Z.N., Woldai, T., van der Meer, F.D., Barongo, J.O., 2010. Active fault segments as potential earthquake sources: inferences from integrated geophysical mapping of the Magadi fault system, Southern Kenya rift. J. African Earth Sci. 57-4, 345–359. https://doi.org/10.1016/j.jafrearsci.2009.11.004.
Last, R., Nyblade, A., Langston, C., Owens, T., 1997. Crustal structure of the east African plateau from receiver functions and Rayleigh wave phase velocities. J. Geophys. Res. Solid Earth 102, 24469–24483. https://doi.org/10.1029/97JB02156.
Laske, G., Masters, G., Ma, Z., Pasyanos, M.E. 2013. Update on CRUST1.0: A 1-degree Global Model on Earth's Crust. Poster EGU2013-2658.
Le Gall, B., Gernigon, L., Rolet, J., Ebinger, C., G loaguen, R., Nilsen, O., Mruma, A., 2004. Neogene-Holocene rift propagation in central Tanzania: morphostructural and aeromagnetic evidence from the Kilombero area. Bull. Geol. Soc. Am. 116 (3-4), 490–510. https://doi.org/10.1130/B25202.1.
Lee, W.H., Uyeda, S., 1965. Review of heat flow data. Terr. Heat Flow 8, 87–190. https://doi.org/10.1029/GM008p0087.
Lenoir, J.L., Liégois, J.P., Theunissen, K., Klerkx, J., 1994. The Palaeoproterozoic Ubendian shear belt in Tanzania: geochronology and structure. J. Afr. Earth Sci. 19 (3), 169–184. https://doi.org/10.1016/0899-5362(94)90059-0.
Li, C.-F., Wang, J., Lin, J., Wang, T., 2013. Thermal evolution of the North Atlantic lithosphere: new constraints from magnetic anomaly inversion with a fractal magnetization model. Geochem. Geophys. Geosyst. 14 (12), 5078–5105. https://doi.org/10.1002/2013GC004896.
Li, C-F., Lu, Y., Wang, J., 2017. A global reference model of curie-point depths based on EMAG2. Sci Rep. 7, 45129. https://doi.org/10.1038/srep45129.
Li, CF., Zhou, D., Wang, J., 2019. On application of fractal magnetization in Curie depth estimation from magnetic anomalies. Acta Geophys. 67, 1319–1327. https://doi.org/10.1007/s11600-019-00339-6.
Liang, W., Li, J., Xu, X., Zhang, S., Zhao, Y., 2020. A high-resolution earth's gravity field model SGG-UGM-2 from GOCE, GRACE, satellite altimetry, and EGM2008. Geodesy Surv. Eng. 6, 860–878. https://doi.org/10.1016/j.eng.2020.05.008.
Lösing, M., Ebbing, J., Szwillus, W., 2020. Geothermal heat flux in Antarctica: assessing models and observations by Bayesian inversion. Front. Earth Sci. https://doi.org/10.3389/feart.2020.00105.
Lysak, S.V., 1987. Terrestrial heat flow of continental rifts. Tectonophysics 143 (1–3), 31–41. https://doi.org/10.1016/0040-1951(87)90076-X.
Manya, S., 2011. Nd-isotopic mapping of the Archaean–Proterozoic boundary in southwestern Tanzania: Implication for the size of the Archaean Tanzania Craton. Gondwana Res 20 (2011), 325–334. https://doi.org/10.1016/j.gr.2011.01.002.
Manya, S., 2001. Geochemical Investigation of Archaean Greenstones in the Rwamagaza Area, North-Western Tanzania. University of Dar-es-Salaam. M.Sc. Thesis.
Manya, S., Maboko, M.A.H., 2003. Dating basaltic volcanism in the Neoarchean Sukumaland Greenstone Belt of the Tanzania Craton using Sm–Nd method: implications for the geological evolution of the Tanzania Craton. J. Afr. Earth Sci. 121, 35–45. https://doi.org/10.1016/S0301-9268(02)00195-X.
Martos, Y.M., Catalán, M., Jordan, T.A., Golynsky, A., Golynsky, D., Eagles, G., Vaughan, D.G., 2017. Heat flux distribution of Antarctica unveiled. Geophys. Res. Lett. 44 (22), 11417–11426. https://doi.org/10.1002/2017GL075609.
Martos, Y.M., Jordan, T.A., Catalán, M., Jordan, T.M., Bamber, J.L., Vaughan, D.G., 2018. Geothermal heat flux reveals the Iceland hotspot track underneath Greenland. Geophys. Res. Lett. 45 (16), 8214–8222. https://doi.org/10.1029/2018GL078289.
Martos, Y.M, Catalán, M., Galindo-Zaldivar, J., 2019. Curie depth, heat flux, and thermal subsidence reveal the Pacific mantle outflow through the Scotia Sea. J. Geophys. Res. Solid Earth 124, 10735–10751. https://doi.org/10.1029/2019JB017677.
Mather, B., Fullea, J., 2019. Constraining the geotherm beneath the British Isles from Bayesian inversion of Curie depth: integrated modelling of magnetic, geothermal, and seismic data. Solid Earth 10, 839–850. https://doi.org/10.5194/se-2019-9.
Maus, S., Dimri, V.P., 1995. Potential field power spectrum inversion for scaling geology. J. Geophys. Res. 100 (B7), 12605–12616. https://doi.org/10.1029/95JB00758.
Maus, S., Gordon, D., Fairhead, J.D., 1997. Curie temperature depth estimation using a self-similar magnetization model. Geophys. J. Int. 129, 163–168. https://doi.org/10.1111/j.1365-246X.1997.tb00945.x.
Meert, J.G., Lieberman, B.S., 2008. The Neoproterozoic assembly of Gondwana and its relationship to the Ediacaran-Cambrian radiation. Gondwana Res 14, 5–21. https://doi.org/10.1016/j.gr.2007.06.007.
Meyer, B., Saltus, R., Chulliat, A., 2017. EMAG2: Earth Magnetic Anomaly Grid (2-Arcminute Resolution) Version 3. National Centers for Environmental Information, NOAA. https://doi.org/10.7289/V5H70CVX.
Mbia, P.K., Mortensen, A.K., Oskarsson, N., Hardarson, B.S., 2015. Sub-surface geology, petrology and hydrothermal alteration of the menengai geothermal field, Kenya: case study of wells MW-02, MW-04, MW-06 and MW-07. In: Proceedings of the World Geothermal Congress 2015. Melbourne, Australia.
Mnjokava, T., Kabaka, K., Mayalla, J., 2015. Geothermal development in Tanzania – a country update. In: Proceedings of the World Geothermal Congress 2015. Melbourne, Australia.
Mole, D.R., Barnes, S.J., Taylor, R.J., Kinny, P.D., Fritz, H., 2018. A relic of the Mozambique Ocean in south-east Tanzania. Precambrian Res. 305, 386–426. https://doi.org/10.1016/j.precamres.2017.10.009.
Möller, A., Mezger, K., Schenk, V., 2000. U-Pb dating of metamorphic minerals: PanAfrican metamorphism and prolonged slow cooling of high pressure granulites in Tanzania, East Africa. Precambrian Res. 104, 123–146. https://doi.org/10.1016/S0301-9268(00)00086-3.
Mpanda, S., 1997. Geological Development of the East African Coastal Basin of Tanzania. Stockholm University, Sweden. Ph.D. ThesisISBN:91-22-01756-9.
Mruma, A.H., 1995. Stratigraphy and palaeodepositional environment of the Palaeoproterozoic volcano-sedimentary Konse Group in Tanzania. J. Afr. Earth Sci. 21 (2), 281–290. https://doi.org/10.1016/0899-5362(95)00065-2.
Mshiu, E.E., Maboko, M.A.H., 2012. Geochemistry and petrogenesis of the late Archaean high-K granites in the southern Musoma-Mara Greenstone Belt: their influence in evolution of Archaean Tanzania Craton. J. Afr. Earth Sci. 66, 1–12. https://doi.org/10.1016/j.jafrearsci.2012.03.002.
Mulibo, G.D., Nyblade, A.A., 2013. The P and S wave velocity structure of the mantle beneath eastern Africa and the African superplume anomaly. Geochem. Geophys. Geosyst. 14 (8), 2696–2715. https://doi.org/10.1002/ggge.20150.
Mulibo, G.D., Nyblade, A.A., 2016. The seismotectonics of southeastern Tanzania: implications for the propagation of the eastern branch of the east African rift. Tectonophysics 674, 20–30. https://doi.org/10.1016/j.tecto.2016.02.009.
Nicholas, C.J., Pearson, P.N., McMillan, I.K., Ditchfield, P.W., Singano, J.M., 2007. Structural evolution of southern coastal Tanzania since the Jurassic. J. Afr. Earth Sci. 48, 273–297. https://doi.org/10.1016/j.jafrearsci.2007.04.003.
Njinju, E.A., Kolawole, F., Atekwana, E.A., Stamps, D.S., Atekwana, E.A., Abdelsalam, M. G., Mickus, K.L., 2019. Terrestrial heat flow in the Malawi rifted zone, East Africa: Implications for tectono-thermal inheritance in continental rift basins. J. Volcanol. Geotherm. Res. 387, 106656 https://doi.org/10.1016/j.jvolgeores.2019.07.023.
Nyabeze, P.K., Gwavava, O., 2016. Investigating heat and magnetic source depths in the Soutpansberg Basin, South Africa: exploring the Soutpansberg Basin geothermal field. Geotherm. Energy 4, 1–20. https://doi.org/10.1186/s40517-016-0050-z.
Nyblade, A.A., 1997. Heat flow across the East African plateau. Geophys. Res. Lett. 24 (16), 2083–2086. https://doi.org/10.1029/97GL01952.
Nyblade, A.A., Pollack, H.N., 1993. A global analysis of heat flow from Precambrian terrains: implications for the thermal structure of Archean and Proterozoic lithosphere. J. Geophys. Res. 98, 12207–12218. https://doi.org/10.1029/93JB00521.
Nyblade, A.A., Pollack, H.N., 1992. A gravity model for the lithosphere in western Kenya and northeastern Tanzania. Tectonophysics 212, 257–267. https://doi.org/10.1016/0040-1951(92)90294-G.
Nyblade, A.A., Pollack, H.N., Jones, D.L., Podmore, F., Mushayandebvu, M., 1990. Terrestrial heat flow in east and southern Africa. J. Geophys. Res. 95, 17371–17384. https://doi.org/10.1029/JB095iB11p17371.
Nwankwo, L.I., 2014. Discussion on: "Spectral analysis of aeromagnetic data for geothermal energy investigation of Ikogosi warm spring – Ekiti State, southwestern Nigeria". Geotherm. Energy 2, 11. https://doi.org/10.1186/s40517-014-0011-3.
O'Donnell, J., Adams, A., Nyblade, A.A., Mulibo, G.D., Tugume, F., 2013. The uppermost mantle shear wave velocity structure of eastern Africa from Rayleigh wave tomography: constraints on rift evolution. Geophys. J. Int. 194, 961–978. https://doi.org/10.1093/gji/ggt135.
Okubo, Y., Matsunaga, T., 1994. Curie point depth in northeast Japan and its correlation with regional thermal structure and seismicity. J. Geophys. Res. 99 (B11), 22363–22371. https://doi.org/10.1029/94JB01336.
Okubo, Y., Graf, R.J., Hansen, R.O., Ogawa, K., Tsu, H., 1985. Curie point depths of the island of Kyushu and surrounding area, Japan. Geophysics 50, 481–489. https://doi.org/10.1190/1.1441926.
Parker, R.L., 1973. The rapid calculation of potential anomalies. Geophys. J. Int. 31 (4), 447–455. https://doi.org/10.1111/j.1365-246X.1973.tb06513.x.
Parker, R.L., Huestis, S.P., 1974. The inversion of magnetic anomalies in the presence of topography. J. Geophys. Res. 79 (11), 1587–1593. https://doi.org/10.1029/JB079i011p01587.
Pilkington, M., Todoeschuck, J.P., 1993. Fractal magnetization of continental crust. Geophys. Res. Lett. 20 (7), 627–630. https://doi.org/10.1029/92GL03009.
Pilkington, M., Todoeschuck, J.P., 1990. Stochastic inversion for scaling geology. Geophys. J. Int. 102 (1), 205–217. https://doi.org/10.1111/j.1365-246X.1990.tb00542.x.
Pilkington, M., Todoeschuck, J.P., 2004. Power-law scaling behavior of crustal density and gravity. Geophys. Res. Lett. 31 (9), L09606. https://doi.org/10.1029/2004GL019883.

Plasman, M., Tiberi, C., Ebinger, C., Gautier, S., Albaric, J., Peyrat, S., Gama, R., 2017. Lithospheric low-velocity zones associated with a magmatic segment of the Tanzanian Rift, East Africa. Geophys. J. Int. 210, 465–481. https://doi.org/10.1093/gji/ggx177.

Quintero, W., Campos-Enríquez, O., Hernandez, O., 2019. Curie point depth, thermal gradient, and heat flow in the Colombian Caribbean (northwestern South America). Geotherm. Energy 7 (1). https://doi.org/10.1186/s40517-019-0132-9.

Ravat, D., Pignatelli, A., Nicolosi, I., Chiappini, M., 2007. A study of spectral methods of estimating the depth to the bottom of magnetic sources from near-surface magnetic anomaly data. Geophys. J. Int. 169 (2), 421–434. https://doi.org/10.1111/j.1365-246X.2007.03305.x.

Reeves, C., De Wit, M., 2000. Making ends meet in Gondwana: retracing the transforms of the Indian Ocean and reconnecting continental shear zones. Terra Nova 12, 272–280. https://doi.org/10.1046/j.1365-3121.2000.00309.x.

Ray, L., Förster, H.J., Förster, A., Fuchs, S., Naumann, R., Appelt, O., 2015. Tracking the thermal properties of the lower continental crust: measured versus calculated thermal conductivity of high-grade metamorphic rocks (Southern Granulite Province, India). Geothermics 55, 138–149. https://doi.org/10.1016/j.geothermics.2015.01.007.

Represas, P., Catalão, J., Montesinos, F.G., Madeira, J., Mata, J., Antunes, C., Moreira, M., 2012. Constraints on the structure of Maio Island (Cape Verde) by a three-dimensional gravity model: imaging partially exhumed magma chambers. Geophys. J. Int. 190, 931–940. https://doi.org/10.1111/j.1365-246X.2012.05536.x.

Rizzello, D., Armadillo, E., Pasqua, C., Pisani, P., Mnjokava, T., Mwano, J., Didas, M., Tumbu, L., 2018. Three-dimensional geophysical modelling of Kiejo-Mbaka geothermal field, Tanzania. In: Proceedings of the ARGEO-C7 Geothermal Conference. Kigali, Rwanda, p. 14.

Ross, H.E., Blakely, R.J., Zoback, M.D., 2006. Testing the use of aeromagnetic data for the determination of Curie depth in California. Geophysics 71, L51–L59. https://doi.org/10.1190/1.2335572.

Salem, A., Green, C., Ravat, D., Singh, H.K., East, P., Fairhead, J., Morgen, D.S., Biegert, E., 2014. Depth to Curie temperature across the central Red Sea from magnetic data using the de-fractal method. Tectonophysics 624–625, 75–86. https://doi.org/10.1016/j.tecto.2014.04.027.

Saria, E., Calais, E., Stamps, D.S., Delvaux, D., Hartnady, C.H., 2014. Present-day kinematics of the East African rift. J. Geophys. Res. 119 (4), 1–17. https://doi.org/10.1002/2013JB010901.

Sclater, J.G., Jaupart, C., Galson, D., 1980. The heat flow through oceanic and continental crust and the heat loss of the Earth. Rep. Geophys. Space Phys. 18, 269–311. https://doi.org/10.1029/RG018i001p00269.

Simiyu, S.M., Keller, G.R., 2001. An integrated geophysical analysis of the upper crust of the southern Kenya rift. Geophys. J. Int. 147, 543–561. https://doi.org/10.1046/j.0956-540x.2001.01542.x.

Simiyu, S.M., Keller, G.R., 1997. Integrated geophysical analysis of the East African plateau from gravity and recent seismic studies. in stress and stress release in the Lithosphere, eds Fuchs, K., Altherr, R., Muller, B. & C., Prodehl Tectonophysics 278, 291–314. https://doi.org/10.1016/S0040-1951(97)00109-1.

Sommer, S., Kröner, A., 2013. Ultra-high temperature granulite-facies metamorphic rocks from the Mozambique Belt of SW Tanzania. Lithos 170, 117–143. https://doi.org/10.1016/j.lithos.2013.02.014.

Spector, A., Grant, F., 1970. Statistical models for interpreting aeromagnetic data. Geophysics 35 (2), 293–302. https://doi.org/10.1190/1.1440092.

Stamps, D.S., Saria, E., Kreemer, C., 2018. A geodetic strain rate model for the east African rift system. Sci. Rep. 8, 732. https://doi.org/10.1038/s41598-017-19097-w.

Stendal, H., Frei, R., Muhongo, S., Rasmussen, T.M., Mnali, S., Petro, F., Temu, E.B., 2004. Gold potential of the Mpanda mineral field, SW Tanzania: evaluation based on geological, lead isotopic and aeromagnetic data. J. Afr. Earth Sci. 38, 437–447. https://doi.org/10.1016/j.jafrearsci.2004.04.005.

Stern, R.J., 1994. Arc assembly and continental collision in Neoproterozoic East African Orogen: implications for the consolidation of Gondwanaland. Ann. Rev. Earth Planet. Sci. 22, 319–351. https://doi.org/10.1146/annurev.ea.22.050194.001535.

Stiefenhofer, J., Farrow, D.J., 2004. Geology of the Mwadui kimberlite, Shinyanga district, Tanzania. Lithos 76, 139–160. https://doi.org/10.1016/j.lithos.2004.04.017.

Tanaka, A., Okubo, Y., Matsubayashi, O., 1999. Curie point depth based on spectrum analysis of the magnetic anomaly data in East and Southeast Asia. Tectonophysics 306, 461–470. https://doi.org/10.1016/S0040-1951(99)00072-4.

TGDC-Tanzania Geothermal Development Company, 2020. Geoscientific Investigation Report for the Ibadakuli Geothermal Prospect, Tanzania. TGDC-Tanzania Geothermal Development Company, p. 44. TGDC Technical internal report (unpublished.

Thomas, R.J., Spencer, C., Bushi, A.M., Baglow, N., Boniface, N., de Kock, G., Horstwood, M.S., et al., 2016. Geochronology of the central Tanzania Craton and its southern and eastern orogenic margins. Precambrian Res. 277, 47–67. https://doi.org/10.1016/j.precamres.2016.02.008.

Thomas, R.J., Bushi, A.M., Roberts, N.M., Jacobs, J., 2014. Geochronology of granitic rocks from the Ruangwa region, southern Tanzania – links with NE Mozambique and beyond. Precambrian Res. 100, 70–80. https://doi.org/10.1016/j.jafrearsci.2014.06.012.

Tiberi, C., Gautier, S., Ebinger, C., Roecker, S., Plasman, M., Albaric, J., Deverch, J., et al., 2019. Lithospheric modification by extension and magmatism at the craton-orogenic boundary: North Tanzania divergence, East Africa. Geophys. J. Int. 216, 1693–1710. https://doi.org/10.1093/gji/ggy521.

TPDC-Tanzania Petroleum Development Company, 2021. Gas Discoveries. TPDC-Tanzania Petroleum Development Company. https://www.tpdc.co.tz/gasdiscoveries.php.

Tugume, F., Nyblade, A., Julia, J., 2012. Moho depths and Poisson's ratios of Precambrian crust in East Africa: evidence for similarities in Archean and Proterozoic crustal structure. Earth planet. Sci. Lett. 355, 73–81. https://doi.org/10.1016/j.epsl.2012.08.041.

Witter, B.J., Miller, A.C., Friend, M., Colpron, M., 2018. Curie point depths and heat production in Yukon, Canada. In: Proceedings of the 43rd Workshop on Geothermal Reservoir Engineering.

Wölbern, I., Rumpker, G., Schumann, A., Muwanga, A., 2010. Crustal thinning beneath the Rwenzori region, Albertine rift, Uganda, from receiver-function analysis. Int. J. Earth Sci. 99, 1545–1557. https://doi.org/10.1007/s00531-009-0509-2.

Wopfner, H., 2002. Tectonic and climatic events controlling deposition in Tanzanian Karoo basins. J. Afr. Earth Sci. 34, 167–177. https://doi.org/10.1016/S0899-5362(02)00016-7.

Further readings

Abraham, E.M, Lawal, K.M., Ekwe, A.C., Alile, O., Murana, K.A., Lawal, A.A., 2014. Spectral analysis of aeromagnetic data for geothermal energy investigation of Ikogosi Warm Spring - Ekiti State, southwestern Nigeria. Geothermal Energy 2, 1–21. https://doi.org/10.1186/s40517-014-0006-0.

Amante, C., Eakins, B.W., 2009. ETOPO1 1 arc-minute global relief model: procedures, data sources and analysis. NOAA Technical Memorandum NESDIS NGDC-24. National Geophysical Data Center, Marine Geology and Geophysics Division, Boulder, Colorado. https://repository.library.noaa.gov/view/noaa/1163.

, UN Environment Africa Geothermal Inventory Database (AGID). https://agid.theargeo.org/countries.php.

Laske, G., Masters, G., Ma, Z., Pasyanos, M.E., 2013. Update on CRUST1.0 - A 1- degree global model of Earth's crust. EGU General Assembly 15, EGU2013–2658. Retrieved from http://meetingorganizer.copernicus.org/EGU2013/EGU2013-2658.pdf.

Plasman, M., Tiberi, C., Ebinger, C., Gautier, S., Albaric, J., Peyrat, S., Gama, R., 2017. Lithospheric low-velocity zones associated with a magmatic segment of the Tanzanian Rift, East Africa. Geophys. J. Int. 210 (1), 465–481. https://doi.org/10.1093/gji/ggx177.